In-Flight Application of Dielectric Barrier Discharge Plasma Actuators for Active Wave Control

Vom Fachbereich Maschinenbau
an der Technischen Universität Darmstadt
zur
Erlangung des Grades eines Doktor-Ingenieurs (Dr.-Ing.)
genehmigte

D i s s e r t a t i o n

vorgelegt von

M.Sc. Armin Kurz

aus Bad Soden am Taunus

Berichterstatter:	Prof. Dr.-Ing. C. Tropea
1. Mitberichterstatter:	Prof. Dr.-Ing. R. King
2. Mitberichterstatter:	Prof. Dr.-Ing. S. Grundmann
Tag der Einreichung:	20.10.2015
Tag der mündlichen Prüfung:	26.01.2016

Darmstadt 2017
(D17)

Hiermit versichere ich, die vorliegende Doktorarbeit unter der Betreuung von Prof. Dr.-Ing. C. Tropea und Prof. Dr.-Ing. S. Grundmann nur mit den angegebenen Hilfsmitteln selbständig angefertigt zu haben.

Darmstadt, den 20.10.2015

Abstract

In the presented study the active closed-loop control of boundary layer disturbances using dielectric barrier discharge plasma actuators is investigated. The main goal of the study was to increase the technological level of the technique and to demonstrate its applicability in flight under realistic atmospheric conditions. For this purpose an experimental setup has been developed, which can be utilized in the wind tunnel, as well as on a GROB G109b motorized glider. The wing glove provides storage space for the necessary data acquisition equipment and features exchangeable measurement inlays housing the actuators and sensors without interfering with the structural integrity of the aircraft's wing. Additionally, the plasma actuator offers two variations in the mode of operation. On the one hand, the direct frequency mode has been investigated, which means the plasma actuator is operated directly at the frequency of the boundary layer disturbances to be controlled. On the other hand, the plasma actuator offers the possibility to combine boundary layer stabilization and active wave control in a single device. This hybrid mode of operation has been successfully investigated during this study for the first time. Boundary layer stabilization is applied by injection of momentum into the lower boundary layer, increasing its local stability. Using adaptive control and suitable flow sensors, the remaining boundary layer disturbances can be further reduced by the principle of negative linear superposition. The energy requirements of the plasma actuator are not significantly altered due to the periodic nature of the additional amplitude modulation as compared to pure boundary layer stabilization. Therefore, the control efficiency is increased. Significant transition delay results could be demonstrated in the wind tunnel, as well as in flight under atmospheric conditions.

Kurzfassung

Die vorliegende Arbeit behandelt die aktive Kontrolle von Grenzschichtinstabilitäten mit Hilfe von Plasma-Aktuatoren basierend auf dielektrischer Barriere-Entladung. Das Hauptziel der Arbeit ist es, die Methode weiter zu entwickeln und deren Anwendbarkeit im Flug unter realistischen, atmosphärischen Bedingungen zu demonstrieren. Zu diesem Zweck wurde ein experimenteller Aufbau entwickelt, welcher sowohl im Windkanal als auch im Flug auf einem der Motorsegler vom Typ GROB G109b zum Einsatz kommen kann. Der Flügelhandschuh stellt dabei den Einbauraum für die notwendige Datenerfassung bereit und wurde mit austauschbaren Einsätzen ausgestattet, die es erlauben Sensoren und Aktuatoren ohne Eingriffe in die Struktur des Flugzeugs zu installieren. Zusätzlich erlaubt der Plasma-Aktuator zwei Variationen seines Betriebsmodus. Zum einen wurde die direkte Frequenzanpassung untersucht, was bedeutet, dass der Plasma-Aktuator direkt mit der Frequenz der Grenzschichtstörungen, die kontrolliert werden sollen, betrieben wird. Zum anderen bietet der Plasma-Aktuator zudem die Möglichkeit eine aktive Grenzschichtstabilisierung mit einer aktiven Wellendämpfung in einem Bauelement zu vereinen. Dieser sogenannte hybride Betriebsmodus konnte erstmals erfolgreich im Zuge dieser Untersuchungen angewandt werden. Die Grenzschichtstabilisierung wird dabei durch die Einbringung eines kontinuierlichen Impulses in die untere Grenzschicht erreicht, wodurch die lokale Stabilität gegenüber Störungen erhöht wird. Unter Zuhilfenahme von adaptiven Regelalgorithmen und geeigneten Strömungssensoren, können dann die verbleibenden Störungen über das Prinzip der negativen Superposition weiter gedämpft werden. Der Energiebedarf des Plasma-Aktuators wird durch die zusätzliche periodische Modulation des Ansteuerungssignals im Vergleich zur Grenzschichtstabilisierung nur unwesentlich verändert. Dadurch ist die Effizienz der Strömungskontrolle erhöht. Signifikante Transitionsverzögerungsraten konnten sowohl im Windkanal, als auch im Flug unter atmosphärischen Bedingungen erzielt werden.

Acknowledgements

The financial support by the Deutsche Forschungsgemeinschaft (DFG) under grant TR 194/39-2 is thankfully acknowledged.

First of all, I would like to thank my doctoral advisors Professor Cameron Tropea and Professor Sven Grundmann for the opportunity to work at the Center of Smart Interfaces and at the Institute of Fluid Mechanics and Aerodynamics. It has always been a great pleasure to work in this professional environment. I would like to express my gratitude to both of them for the excellent supervision and ongoing support.

I am particularly grateful to Professor Rudibert King for the collaboration regarding this research project and for his commitment to referee my thesis. In the same manner I am grateful to Dr.-Ing. Nikolas Goldin. His feedback and the fruitful discussions have contributed a lot to the outcome of this experimental study.

Without the team involved with the flight experiments and the operation of the aircraft, it would not have been possible to conduct the in-flight measurement campaigns. I would like to thank Alexander Duchmann, Markus Jenkner, Andreas Reeh, Günther Schapka, Bernhard Simon, Martin Stenger, and Michael Weismüller for their support.

Some of the experiments presented in this work have been conducted at ONERA Toulouse. It has been a memorable experience for me to visit this great facility. I would like to express my gratitude to the whole team, especially Maxime Forte and Olivier Vermeersch.

Sincere thanks to Ilona Kaufhold and her team of the mechanical workshop and to Martin Weiss for the support while building the experimental setups and for their commitment to keep the wind tunnels running. I am also very thankful to Matthias Quade, who was always willing to help with wind tunnel issues, even when the hour was getting late.

Furthermore, I am thankful to my colleagues for their friendship and for the great working environment in Griesheim. Also I would like to thank Débora Vieira for sharing her numerical expertise.

Finally, I am truly thankful to my wife and my family for their encouragement and support throughout the whole time.

Contents

1 Introduction

1.1 History of Plasma Actuator Research

Plasma discharges as a possible means of flow control already appeared in the literature as early as the 1950s. Early work was mainly focused on corona wire discharges, as for example documented in [59]. In this work a wire-to-plate discharge, driven by a DC potential, was utilized for transition control purposes on a flat plate flow. The discharge induced a secondary velocity component, acting on the stability of the boundary layer. A transition delay effect is reported up to a free stream velocity of $U_\infty = 175 fps$. The transition delay effect was found to be independent of the applied discharge frequency ranging from continuous to 6kHz.

After this early publication only a few studies on the subject appeared until the mid-1990 as comprehensively reviewed in [42]. At this time the plasma actuator emerged as a flow control device following the work of Roth, who first developed his device as a ozone generator for decontamination and surface treatment. In contrast to the corona discharge, this actuator consists of two asymmetrically positioned electrodes, which are separated by a dielectric material, hence the name dielectric barrier discharge (DBD) plasma actuator. Realizing that the operation of the actuator induces a secondary flow, the use as a flow control device was proposed. The results of this work were published in [51, 52]. Since this time, the use of surface-mounted, non-thermal plasma actuators has gained widespread interest in the research community, owing to their apparent advantages. Very appealing is its feature to transport momentum into the flow without the need of any moving parts and the low space requirements of the actuator itself. Basically it can be integrated in almost any non-conducting aerodynamic surface by flush-mounting it into a shallow groove. This is in contrast to many other zero-net mass-flux control devices, like cavities driven by loudspeakers or piezo-electric devices. In this case considerable volume is required inside of the structure to house the devices and in addition, the structure usually is weakened by necessary exit holes or slots to introduce the momentum into the flow. Very important in this context is

the fact, that due to the absence of any moving parts, the plasma actuator does not by itself introduce unwanted vibrations into the aerodynamic structure and therefore into the flow. Under adverse conditions unwanted surface vibrations could have a detrimental effect on the flow control efficiency. DBD plasma actuators exhibit a fast response time, which is advantageous when applying them to active wave cancelation. The plasma actuator itself is light-weight and also compact, light-weight, high-voltage power supplies are available nowadays, promoting an in-flight application of the device.

The research efforts following the mid-1990s can be subdivided in two areas. One group of researchers aimed on the understanding of the underlying physical mechanisms by experimental and numerical means, which could explain the directed momentum production of the plasma actuator. The other group concentrated on the application of the plasma actuators to a wide range of flow control problems. During the process of investigating the underlying physics it has been discussed controversially, if the volume force of the plasma actuator is directed downstream only during the negative half-cycle of the discharge and is small, but directed upstream, during the positive discharge half-cycle, or if it is directed downstream during both half-cycles. This led to the well known "push-push" and "push-pull" theories. In addition, it was not fully understood how the ions interact in detail with the neutral molecules of the ambient gas, leading to the development of complex numerical models of the plasma actuator [7, 8, 10, 22]. This was accompanied by experimental work applying PIV and also LDA in close vicinity of the plasma region in order to measure the induced velocities directly and, in the case of PIV, determine the resulting body force from field data [25, 40, 63]. These studies confirmed the pulsed nature of the momentum production. The large parameter space and the relatively low control authority, i.e. the relatively low induced velocity close to the wall, also triggered extensive parameter studies involving the influence of the ambient pressure, the gas species present in the flow, as well as the influence of electrode geometry and material [1]. The goal of these studies has been to find a suitable field of application and the optimization of the plasma actuator for flow control purposes [23].

The efforts to improve the performance of the plasma actuator also lead to novel electrode configurations, like for example the so called sliding discharge, where the standard actuator with two asymmetrically positioned electrodes is accompanied by a third electrode some distance downstream. At this third electrode a DC potential is applied, improving the acceleration

of the ions in the plasma region and therefore improving the momentum production [43].

In order to improve the momentum transfer to the fluid it has also been considered to built arrays of continuously operating plasma actuators, but if arranged closely, cross-talk between the actuators takes place, which results in unwanted upstream oriented plasma, which significantly deteriorates the performance. As an elegant solution it was suggested to apply various three-electrode configurations, shielding each actuator from the following one effectively [5]. Alternatively, it is also possible to apply the common two-electrode configuration and switch the connection to high-voltage and ground for each pair in an alternating fashion. The research on sliding discharge, streamer inhibition by the use of thin wire electrodes for the exposed electrode and electrode configurations, as well as optimizing the electrical input signal is still ongoing [6, 14, 15].

The plasma actuator also has some apparent disadvantages, which have to be mentioned. The inevitable production of ozone when operating a plasma actuator in air can lead to a deterioration of the electrode material, as well as of the dielectric material, limiting the lifetime of the devices. The durability is depending on several factors, like the used materials for electrode and dielectric material, the operating conditions, especially the applied high voltage, and also on the environmental conditions like ambient pressure, temperature, humidity and the composition of the surrounding gas. Novel materials have been investigated at the Technische Universität Darmstadt and among other groups. Advancements in the area of material sciences will very likely increase the applicable voltage range and the lifetime of the devices in the future.

The body forces generated by a DBD plasma actuator are relatively low compared to other fluidic flow control devices. This shortcoming has to be overcome in the next years, if plasma actuators are to be considered as a promising flow control device in large scale applications. This is certainly true, if the PA is considered for flow control applications that require high momentum input. Nevertheless, the plasma actuator is an ideal device for transition control, since only small momentum inputs are necessary to influence the disturbances present in a laminar boundary layer, like in the case of active wave cancelation. This is in contrast to applications, which are based on a mean flow modification.

1.2 State of the Art of Plasma Actuator Flow Control

Parallel to the efforts explaining the underlying physics of the plasma-actuator, within a short period of time, many experimental studies emerged applying the plasma actuator to a variety of flow control problems. There are several areas of interest, when considering plasma-actuators for flow control: laminar-turbulent transition, separation control and even the manipulation of turbulence.

Among the applications that have been investigated are for example cylinder wake control [37], the use of the plasma actuator as a vortex generator for separation control [38], active separation control on NACA airfoils [39], stall control and lift enhancement on an airfoil applying the actuator to leading and trailing edge [13], lift enhancement and roll control [61]. The efforts regarding actuator physics, modeling and the different applications have been summarized in extensive reviews [12, 42].

Active wave control and boundary layer stabilization using DBD plasma actuators as flow control device were introduced by Grundmann and Tropea in 2007 [31]. Both transition control methods have been successfully applied during this study. First, the plasma actuator can be operated continuously adding a continuous momentum to the lower boundary layer. This way the stability features of the boundary layer are altered such that the development of boundary layer disturbances and therefore the transition to turbulence is delayed. On the other hand the DBD plasma actuator can be operated in a pulsed mode of operation in order to generate flow structures within the boundary layer with properties similar to TS waves. By careful adjustment of amplitude and phase a wave attenuation can be achieved by the principle of linear negative superposition. An active control circuit is necessary in this case. Other groups reported successful transition control experiments using plasma actuators as well. Seraudie et al. reported on natural transition delay on a flat plate applying boundary layer stabilization [55, 56].

Despite all of these achievements, the plasma actuator is still undergoing a research phase, as compared to other actuators and methods which have reached a higher level of maturity and application.

1.3 Motivation

The aim of the present research project is to raise the technological level of active wave control using DBD plasma actuators. For this purpose it is necessary to further investigate the transition control mechanisms and the modes of operation of the plasma actuator in the wind tunnel. Additionally, in-flight experiments are pursued in order to take first steps towards the control of TS wave induced transition under realistic, atmospheric conditions.

One of the challenges is to reduce the energy necessary for achieving a delayed transition as compared to previous works. This requires the application of more sophisticated mechanisms such as AWC. These in turn require sensing of boundary layer disturbances and sophisticated control algorithms. Furthermore, a substantial increase in the applicable Reynolds number range is necessary. In order to achieve these goals, the following steps have been identified:

- Design of an in-flight testing platform using an aerodynamic profile
- Design of a suitable disturbance source for wind tunnel as well as for in-flight usage
- Application of more efficient control algorithms in a real-time environment
- Proving of flow sensors for the use in combination with plasma actuators
- Flight tests with the newly developed experimental setup

Two interesting variations in the mode of operation using plasma actuators as a flow control device have been investigated during the course of this study. On the one hand, the so called hybrid mode of operation has been demonstrated, which combines the boundary layer stabilization by continuous momentum addition with an effective wave cancelation using a modulated momentum input. On the other hand, it is possible to operate the plasma actuator directly at the frequency of the boundary layer disturbances, which is called the direct frequency mode. This is particularly of interest when an increase in free-stream velocity and Reynolds number

is desired up to a point, where the momentum pulses cannot be modeled with sufficient resolution anymore using a carrier frequency. This is the case, when the frequency of the boundary layer disturbances and the carrier frequency of the plasma actuator are of the same order.

1.4 Thesis Organization

Chapter 1:
A brief summary of the history regarding research on plasma actuators is given. The most important research groups, who have contributed to the understanding and the development of the various devices are discussed. Furthermore, focus is on the state of the art in flow control using plasma actuators. This leads to the key questions and the motivation for the presented study.

Chapter 2:
In this section an overview of the necessary background regarding plasma actuators is given. The working principle of the plasma actuator is briefly discussed and possible transition delay mechanisms in wall-bounded flows, as well as the modes of operation, are explained. The fundamentals of control theory relevant for this study are introduced to motivate the use of feed-forward control.

Chapter 3:
The experimental setups and the facilities that have been utilized throughout the course of the wind tunnel campaigns, as well as the in-flight setup and the GROB G109 motorized glider are presented. This chapter includes sensors and actuators and the applied measurement techniques.

Chapter 4:
In chapter 4 the most important results of the wind tunnel experiments are presented. Experiments investigating the direct frequency mode to directly drive the actuator at the TS wave frequency are included here. This study has been conducted within the framework of the European project PLASMAERO at the facilities of ONERA Toulouse. This is followed by the wind tunnel investigations on the hybrid mode of operation and the preparation of the flight campaign.

Chapter 5:
This section summarizes the results of the in-flight experiments using the newly developed flight setup. The Reynolds number range using plasma actuators for transition control could be expanded to $Re = 3.0 \cdot 10^6$. Also in flight significant transition delay results could be obtained, which demonstrates the potential auf the hybrid mode of operation for plasma actuators.

Chapter 6:
In conclusion the most important results of the work are reviewed and discussed. In the outlook possibilities and suggestions for future improvements are given.

2 Background

2.1 Transition Control Mechanisms using DBD Plasma Actuators

Basically two fundamental transition control methods can be distinguished, when single DBD plasma actuators are utilized for the purpose of transition control. Boundary layer stabilization can be characterized as an indirect method. It acts on the local stability features of the boundary layer. This in return changes the unstable frequency range of the boundary layer and therefore prevents the amplification of boundary layer instabilities. On the other hand, active wave cancelation directly acts on the velocity fluctuations present in the boundary layer and directly dampens them. This method is not based on the modification of the boundary layers' stability. The plasma actuator also allows for a intentional combination of these two mechanisms, which is called hybrid transition control mode. To explain these effects in detail, the transition control mechanisms and the working principles of the different modes are introduced and compared in this section.

2.1.1 Mean Flow Modification

The active stabilization of a boundary layer using DBD plasma actuators is the more forward application of the two methods. The actuator is operated in a continuous fashion, injecting a quasi-steady momentum into the lower boundary layer.

It is well known that the body force generation of a plasma actuator is highly unsteady during each cycle of the applied high alternating current, as for example shown in [9]. Due to the mass inertia of the fluid a quasi-steady, wall-parallel velocity can be observed, but a certain amount of unsteadiness remains in the secondary flow. Therefore, the frequency of the carrier signal driving the plasma actuator has to be located well outside of the unstable frequency band of the flow, which is usually the case in low Reynolds number flows. Whereas the carrier frequency is in the range of $10^4 Hz$ or higher, the unstable frequencies in the flow are usually about one

order of magnitude lower. Otherwise the plasma actuator would by itself trigger unwanted disturbances. At first sight this is limiting the applicable Reynolds number range for transition control application, unless this carrier frequency could be avoided running the plasma actuator directly at the frequency of the disturbances.

The velocity profile generated by the actuator is superimposed with the boundary layer profile. Even though the deformation of the velocity profile is small, it affects the local stability features of the boundary layer largely. The effect can be shown using linear stability theory.

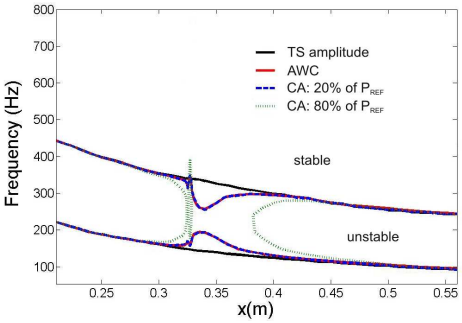

Figure 2.1: Effect of continuous actuation (CA) and active wave control (AWC) of a plasma actuator on the neutral stability curve of a flat plate boundary layer. (Numerical results by D. Vieira [60])

Figure 2.1 shows the effect of a continuously operated plasma actuator (CA) on the local stability behavior of the flow. The data has been obtained using a stability code developed by [16]. Shown is the unstable frequency range along the chord of a flat plate. The plasma actuator is located at $x = 0.325m$. The local effect of the actuation on the amplification of the different frequencies can be observed. For this numerical study a body force has been introduced to the flow field in order to simulate the effect of a plasma actuator. The force distribution has been obtained from PIV experiments performed by [40]. P_{REF} is defined as a body force corresponding to a plasma actuator running continuously at $V_{pp} = 8kV$, which results in integral volume forces of $F_x = 1.88N/m^3$ and $F_y = 1.58N/m^3$. In the actuated case, the unstable frequency band narrows (CA: 20% of P_{REF}) or can be even interrupted using a higher power setting (CA: 80% of P_{REF}), such that the growth of instabilities within the boundary layer

is shifted downstream. The diagram also illustrates that the actuation acts on a broad range of unstable frequencies. Boundary layer stabilization acts on the stability of the boundary layer and therefore modifies the amplification of the boundary layer disturbances. This control method has been applied in several experimental studies [17, 34, 56].

In general, within the operating limits of a plasma actuator, applying a higher horizontally orientated body force leads to a higher stabilizing effect. Even though the stabilization is a local effect, it is noticeable over several TS wave lengths downstream of the actuator and is therefore more distributed than in the case of active wave cancelation. The boundary layer stabilization is ideal for the application in arrays using several actuators distributed in downstream direction. The correct streamwise placement of the actuator is crucial for the success of the transition control, because once the amplitude of the boundary layer disturbances reaches the limit of the linear regime, the achievable transition delay deteriorates.

The stabilizing effect on the boundary layer is independent of the presence of TS waves in the flow. There is no detrimental effect if the actuator is operated and no disturbances are present (apart from the wasted control energy). This means a two-dimensional actuator can be applied to artificially excited two-dimensional TS waves in the same way as to naturally occurring TS waves, which travel in packets. These packets usually are of mixed frequency content and the spanwise location of their occurrence varies randomly. This universal applicability of the boundary layer stabilization using DBD plasma actuators is in contrast to the active wave cancelation.

2.1.2 Direct Cancelation of Disturbances

Much more demanding is transition control by active wave cancelation using plasma actuators. This method exploits the phenomenon of linear negative superposition. The incoming TS wave or the TS wave packets are detected and a suitable counter wave is generated by the control actuator. Ideally, both waves would then cancel each other completely at the location of interaction. This principle has been demonstrated in numerous experimental studies, albeit actuators other than the plasma actuator have been used [29, 32, 47].

This method involves the use of a fast control circuit, which continuously adjusts amplitude, frequency and phase relation of the counter wave in order to effectively remove the TS disturbances from the boundary layer. In the case of artificially excited, mono-frequency TS waves a relatively

simple extremum seeking controller is sufficient, but even in this case an adaptive feed-forward control circuit is expected to perform better, since it includes the actuator characteristics by modeling. In the case of the control of naturally occurring boundary layer disturbances, the use of an adaptive feed-forward control circuit using an upstream reference sensor is mandatory. Suitable flow sensors have to be chosen, which have a sufficient signal-to-noise ratio and, equally important, are insensitive to electromagnetic noise emitted by the plasma actuator.

The necessary detection of the boundary layer disturbances implies that AWC can only act on disturbances that have already been amplified over a considerable downstream distance, until an amplitude level has been reached that is sufficient for the flow sensors. Nevertheless, these disturbances still have to be in their linear amplification stage for an effective control. This suggests that a correct actuator placement is equally important, as compared to the boundary layer stabilization.

In contrast to the boundary layer stabilization, AWC is not based on the modification of the boundary layers stability features. Therefore the effectiveness of the control cannot be predicted using linear stability theory. However, even though small, a pulsed or sinusoidally modulated operation of a plasma actuator also leads to a constant wall-parallel momentum production, which is obvious, if one considers the unidirectional force production of the device. This effect is also visible in Figure 2.1. An active wave cancelation with optimized settings in terms of transition delay also leads to a small stabilizing effect, which is comparable to a continuous actuation at 20% of the reference value, which corresponds to a low high-voltage. This implies that a pure active wave cancelation is not feasible using a plasma actuator and is always combined with a small favorable effect on the boundary layer stability features.

The different effects of active wave control and continuous actuation on TS waves are illustrated in Figure 2.2. Shown is the amplitude distribution along a flat plate Blasius boundary layer under the influence of a local body force located at $x = 0.325m$. As a reference the uncontrolled amplitude development ist included. It can be seen that in the numerical simulation the damping effect of AWC begins directly downstream of the actuator and is a local effect. Downstream of this region the amplitude of the disturbances starts to increase again. In contrast to that, the damping effect of boundary layer stabilization is distributed over a larger downstream region.

The plasma actuator has proven to be very effective in controlling two-dimensional, artificially excited TS waves using AWC. Compared to bound-

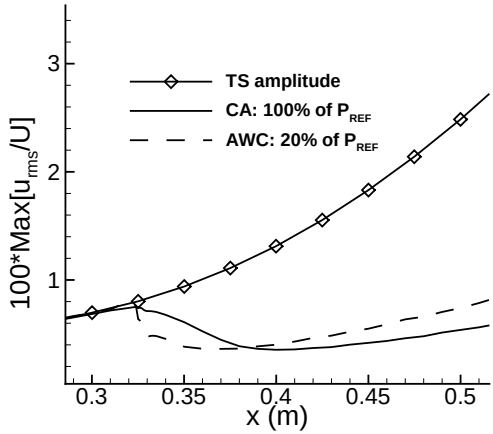

Figure 2.2: Amplitude development of TS waves along a flat plate. Undisturbed growth (waves), continuous actuation (CA) and active wave control (AWC).(Numerical results by D. Vieira [60])

ary layer stabilization, this method is energetically more efficient.

The application of AWC to naturally occurring TS waves involves some challenges. Naturally occurring TS wave packets have a limited spanwise extent in the order of their wave length. Since this method relies on the detection of the incoming disturbances upstream of the actuator, the calculated control parameters are only valid in a narrow corridor downstream of the respective sensor. This makes an actuator array necessary, which is segmented in spanwise direction with an independent actuation per segment. Such an extension of the procedure is not part of this study. Therefore it was decided to artificially excite two-dimensional TS waves with constant properties along the spanwise direction in order to conduct the experiments described in this work.

2.1.3 Hybrid Mode of Operation for DBD Plasma Actuators

Figure 2.3 compares the different possible operating modes of a DBD plasma actuator in relation to a generic TS wave signal. In continuous mode an alternating high-voltage with a fixed carrier frequency is applied

(Fig. 2.3(b)). This frequency is usually adjusted to the resonant frequency of the system comprised of the high-voltage generator and the actuator, resulting in the highest electrical efficiency. The result is a wall parallel body force modulated at the carrier frequency. Usually this frequency is high enough, such that the momentum can be considered as steady for most flow control applications.

For active wave cancelation the carrier signal is amplitude modulated according to frequency, amplitude and phase of the incoming TS waves (Fig. 2.3(c)). The average applied voltage and the power consumption are typically much lower in this case, since the flow control effect is not based on momentum addition, but on the excitation of unstable modes in the flow.

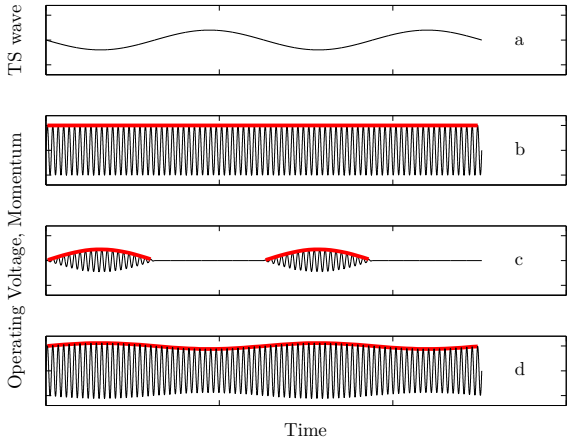

Figure 2.3: Operating modes for the plasma actuator in relation to a TS wave signal (a): b) Continuous mode, c) active wave cancelation, d) hybrid mode. Shown are (qualitatively) the operating voltage (black) and the momentum production over time (red).

In order to run the plasma actuator in hybrid mode both working principles are combined in one actuator. A small amplitude modulation is applied, while the actuator is running continuously at a high peak-to-peak voltage (Fig. 2.3(d)). The result is a body force that induces a substantial amount of momentum to achieve a boundary layer stabilization and this force is simultaneously modulated such that additionally an active wave cancelation is performed.

As outlined in the previous section, pure AWC is not feasible using DBD plasma actuators. There always will be a small continuous wall-parallel component present in the signal. But exactly this inherent downstream velocity component of the momentum generation makes the plasma actuator an ideal candidate for the combination of boundary layer stabilization and active wave cancelation.

In order to conduct AWC in low Reynolds number flows, relatively small momentum inputs are sufficient in order to produce the velocity fluctuations necessary to create the counter wave for linear superposition. Combining both methods of transition control, the plasma actuator is driven in a continuous fashion, in the same way as for boundary layer stabilization. The carrier signal is then amplitude modulated in order induce the velocity fluctuations for the active wave control.

Combining AWC with boundary stabilization has several advantages compared to the individual methods. When pulsing a plasma actuator or when modulating it such that the momentum production is varied periodically between zero and a maximum value, the high voltage falls below the ignition voltage during each control cycle. At the ignition voltage, the plasma is unstable and variations in the force production can occur in spanwise direction. Additionally, the system plasma actuator in conjunction with the high voltage source exhibits a certain transient oscillation behavior when turning the plasma actuator on and off, as described in [2]. The post-pulse oscillation behavior is more pronounced. Both phenomena cannot be avoided and deform the intended control signal, even though it has to be said, that the largest portion of the post-pulse oscillation occurs at a voltage level, which should not result in a discharge and therefore will not create an unwanted momentum production. Modulating the carrier signal at a high continuous level avoids both issues. The representation of the desired body force is much more exact, which in return improves the transition control result.

Another advantage of this method is the additive effect of the amplitude attenuation rates. It is known that the momentum production of single DBD plasma actuators is somewhat limited. Even though some improvements have been published recently, the maximum achievable wall-parallel velocity of a plasma actuator seems to be limited to about $10m/s$. This issue together with the limited durability of the devices sparked an intense discussion about the control authority of the plasma actuator. The applicable Reynolds number range has to be improved to bring the device closer to a practical application. When applying the plasma actuator for boundary

layer stabilization and AWC separately in Reynolds number regimes relevant for in-flight application, for both methods the wave attenuation rates and achievable transition delay rates are limited.

The hybrid transition control mode combines the positive effects of both methods in a favorable way. Continuous forcing stabilizes the boundary layer and results in a given wave attenuation rate. Adding the active wave control results in a larger attenuation rate as compared to individual methods. Interestingly, this improvement comes without increased energy requirements, because the sinusoidal modulation of the carrier signal basically does not change the average value of the consumed power significantly.

When applying a single DBD plasma actuator for active wave cancelation, is is assumed that the level of three-dimensionality of the flow is raised to some extent at the location of the actuator. This is supported by the observation that AWC cannot be repeated indefinitely, when applying streamwise arrays of actuators to flat plate flow. Combining the AWC with boundary layer stabilization helps to alleviate this detrimental effect as well due to the locally increased stability of the boundary layer.

2.2 Control Approach

2.2.1 Active Control of Tollmien-Schlichting Instabilities

For the active control of Tollmien-Schlichting instabilities within a boundary layer several control approaches can be used and have been investigated numerically, as well as experimentally throughout the years. From an experimental point of view it is in many cases mandatory to establish repeatable and controlled conditions. This can be useful for example when investigating the fundamental underlying mechanisms of the interaction between a fluidic actuator and the incoming boundary layer disturbances, or in the design phase of a new experiment. In these cases mono-frequency two-dimensional TS waves of constant amplitude can be introduced into the boundary layer. In order to control such a flow situation an extremum seeking control approach is sufficient. It is well suited for the control of this kind of periodic disturbances and has the advantages of simplicity and robustness.

Since the phase shift between TS waves and the counter waves created by the actuator is the most sensitive parameter in order to achieve a good damping rate, more sensitive than for example the amplitude, it is chosen as the controlled variable. A cost functional is minimized at the position

of the error sensor. A single error sensor positioned downstream of the actuator is sufficient in this case. This sensor can also be traversable, hence promoting a setup, which can be adapted to different requirements with considerable ease.

The control of two-dimensional TS waves of mixed frequency and amplitude content is more involved. In this case upstream information of the incoming disturbances is necessary, which demands the use of a flush-mounted wall sensor in order not to disturb the flow downstream of this location and a feed-forward control has to be applied. The use of such a controller can also be useful in cases of mono-frequency TS waves when freestream disturbances trigger additional disturbances within the boundary layer, which cannot always be avoided in a wind tunnel environment.

The same kind of controller can be applied, when the step is made to control three-dimensional boundary layer disturbances or even naturally occurring TS waves. The challenge here lies in the streamwise and spanwise cascading of the actuators. With the number of control circuits and flow sensors the complexity and the required computational power increases tremendously. Especially so, when interconnection between the individual controllers is taken into consideration.

At the Chair of Aerodynamics and the Chair of Measurement and Control of the Technische Universität Berlin a set of powerful control algorithms has been developed, which is tailored towards the control of boundary layer instabilities. These control algorithms have proven their capabilities within several experimental studies [3, 4, 29, 47, 57] and have reached a high level of development.

In collaboration with the latter group, two control schemes have been implemented to the experimental setup presented within this study. An extremum seeking approach based on an extended Kalman filter (EKF) has been adopted in the design stages of the experiment, in order to control two-dimensional mono-frequency TS waves. Later on, for the control of boundary-layer disturbances with mixed frequency content, as well as for the in-flight experiments an adaptive feed-forward approach (filtered-reference LMS) has been utilized. Both algorithms have been provided for this study and are described briefly in the following sections.

2.2.2 Extremum Seeking Control

The active cancelation of TS waves depends on the generation of a counterwave of the same frequency Ω with the correct phase ϕ and amplitude a. Even though it is possible to set these parameters manually for a continu-

ous wave train, a self-tuning setup is necessary for more realistic conditions of naturally occurring rather than artificially excited TS waves. Therefore a modified extremum seeking control algorithm based on an extended Kalman filter (EKF) has been employed. This method uses a perturbation of the optimization parameter to automatically optimize a cost functional dependent on this parameter. However, this control approach is only applicable for continuous wave trains as presented in this study.

Since the phase relation between the disturbance and the counterwave is the most critical parameter, extremum seeking control is applied to this variable alone. An input $v = a\sin(\Omega t + \phi)$ is used, where $u = \phi$ is the optimized parameter. Note that v only represents the modulated input, to which the constant offset still has to be added. As a cost functional, we use the remaining disturbance at the error sensor, as characterized by the root-mean-square (RMS) value of the sensor signal, $y = e_{\mathrm{RMS}}$.

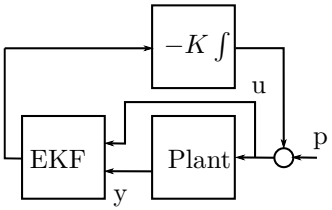

Figure 2.4: Principle of extremum seeking control.

The goal is to automatically find the value of u which minimizes y. For this, it is assumed that the slow behavior of the system can be approximated by an equilibrium input-output map $y = F(u)$, such that $\lim_{t\to\infty} y(t) = y$ for $u(t) = u = const$. This way, the problem is reduced to finding the minimum of a static map. This is achieved by adding a sinusoidal perturbation to u which varies slower than the dynamics of the system. This perturbation can be used to estimate the gradient $\partial y/\partial u$. With this estimation, a gradient descent approach with fixed step size parameter K is used to find the minimum.

For the estimation of the gradient, a modified version of the approach proposed by [36] is used. An extended Kalman Filter (EKF) based on the model of a static process is used for the estimation. However, while [27] uses two time-shifted pairs (u, y) as inputs, here a third pair is added in order to guarantee observability of the system at all times. For a detailed

description of this controller and the applied modifications, the reader is referred to [28].

Figure 2.4 shows the schematic of the extremum seeking control with EKF. The use of a Kalman Filter instead of the classical correlation method has the advantage of increased convergence speed for many systems.

2.2.3 Adaptive Feed-Forward Control

In this section a short introduction to adaptive feed-forward control is given. As mentioned earlier applying this type of control is more involved, since upstream flow information is necessary in order to calculate the control input for the actuator. In return this method also allows to control incoming disturbances of mixed frequency content or intermittently occurring disturbances traveling in packets. Finally the implementation on the wing glove is explained. The description in this section is mainly following the outline given in [20].

2.2.3.1 Single-Input Single-Output (SISO) Systems

The systems discussed in this work are of single-input single-output (SISO) type. This means they consist of a single reference sensor, a single error sensor, as well as a single actuator. In the cases where transition control using two plasma actuators is conducted, each one of them resembles a SISO system as well. Each of them operates independently using an individual control algorithm. The sensors are partially shared in this case, for example the error sensor of an upstream plasma actuator can be used as reference sensor for the next actuator downstream of this location.

Figure 2.5 illustrates the system resembling the experimental setup on the wing glove. Two flush-mounted surface hotwire sensors are utilized as upstream reference and downstream positioned error sensor, respectively.

P_e is called the primary disturbance path and describes the transmission behavior from reference to error sensor. The secondary or error path G_e models the transmission between actuator and error sensor. The response of this path is dependent on the particular flow condition and therefore has to be identified for each operating point.

2.2.3.2 Finite Impulse Response (FIR) Filter

Adaptive digital filters are oftentimes used to form an internal model of the response of a physical system. The objective is the identification of

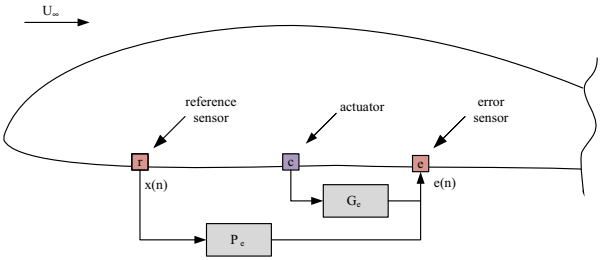

Figure 2.5: Wing glove SISO system with disturbance and error path.

the filters response and to find a set of optimum filter coefficients, such that a mean-square error criterion is minimized automatically. For finding optimum filter coefficients the LMS algorithm is a popular method, which is a form of steepest descend algorithm.

In general, a discrete-time system can be described as input $x(n)$, a transfer function H and an output y(n). If the system is linear, the principle of superposition has to be fulfilled, which means H can be expressed as a linear summation. If the system is a causal linear system, the output is influenced by every previous input, such that the output can be written as the following infinite summation:

$$y(n) = \sum_{i=0}^{\infty} h_i x(n-i) \tag{2.1}$$

The impulse response h_i of the digital system is the response to a Kronecker delta function $x(n) = \delta(n)$, which is equal to 1 for $n = 0$ and equal to zero otherwise.

$$\delta(n) = \begin{cases} 1 & n = 0 \\ 0 & n \neq 0 \end{cases} \tag{2.2}$$

$$y(n) = \sum_{i=0}^{\infty} h_i \delta(n-i) = h_n \tag{2.3}$$

with $n = 0$ to ∞.

In order to apply a digital filter in practice, the calculation of an output sequence may only take a finite amount of time. A common practice is the truncation of the infinite summation.

$$y(n) = \sum_{i=0}^{I-1} w_i x(n-i) \tag{2.4}$$

where w_i are the coefficients, or weights, of the digital filter. The number of coefficients is given by I. In order to allow for computing time at least one sample of delay has to be implemented:

$$y(n) = \sum_{i=1}^{I} w_i x(n-i) = \mathbf{w}^T \mathbf{x}(n) = \mathbf{x}^T(n)\mathbf{w} \tag{2.5}$$

Like with any linear time-invariant (LTI) system, the impulse response of a FIR filter fully describes its behavior and is composed of the filter coefficients.

2.2.3.3 Adaptive Filters

Adaptive filters are systems where an online adjustment of the system parameters is performed according to the characteristics of the signal. Different kinds of filters can be utilized for this purpose. Oftentimes FIR filters are implemented, since they have the advantage of inherent stability. Figure 2.6 illustrates the basic architecture of such an adaptive filter as block diagram. In this case, the coefficients $w_i(n)$ of the FIR filter are adjusted continuously by a suitable adaptive algorithm. This means that the reference signal $x(n)$ is filtered, such that the output signal of the adaptive filter $\hat{d}(n)$ is an accurate estimate of the desired signal $d(n)$. The goal of this adaptation is the minimization of the error (Equation 2.6) with respect to a suitable measure [20], [28], [35].

$$e(n) = d(n) - \mathbf{x}^T(n)\mathbf{w} \tag{2.6}$$

With regard to the practical implementation on the wing glove experiment, $d(n)$ corresponds to the incoming TS wave, $\hat{d}(n)$ is the desired counter wave, $x(n)$ and $e(n)$ correspond to the signals obtained by the upstream reference and downstream error sensor, respectively.

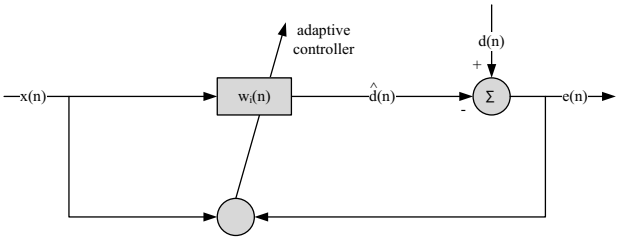

Figure 2.6: Block diagram of an adaptive filter [20].

2.2.3.4 The Least-Mean-Square (LMS) Algorithm

It is possible to calculate a set of optimum filter coefficients, a procedure which has been pioneered by the work of Wiener (Wiener formulation). Knowing the auto-correlation properties of the reference signal and the cross-correlation between reference and desired signal, these coefficients can be obtained. But time series of the signals have to be available for the estimation, which can result in large memory requirements, and the necessary inversion of the auto-correlation matrix can cause considerable computational expense.

Instead of instantaneously calculating the optimum filter coefficients, another possibility is to make the filter coefficients adaptive. This way, sensor data is used sequentially to gradually adjust w_i in order to minimize the mean-square error. Therefore, for application often a running quadratic error $e^2(n) = (d(n) - \mathbf{x}^T(n)\mathbf{w}(n))^2$ is used as cost function. This way no previous data sets are necessary for the calculation, which could lead to a low update frequency, and the coefficients can be adjusted for every time step. For the minimization of the cost function a steepest descend algorithm is used. It may be written as

$$\mathbf{w}(new) = \mathbf{w}(old) - \mu \frac{\partial J}{\partial \mathbf{w}}(old) \tag{2.7}$$

where μ is the convergence factor. Using this procedure, the gradient of the cost function can be written as shown in Equation 2.8 and the adaptive

algorithm takes on the form shown in Equation 2.9, which is commonly known as the LMS algorithm. $\alpha = 2\mu$ is called the convergence coefficient and J is the cost function. The LMS algorithm is widely used, for example in the field of adaptive noise cancelation.

$$\frac{\partial e^2(n)}{\partial \mathbf{w}} = -2\mathbf{x}(n)e(n) \tag{2.8}$$

$$\mathbf{w}(n+1) = \mathbf{w}(n) + \alpha\mathbf{x}(n)e(n) \tag{2.9}$$

The second term of Equation 2.9 represents the modification of the filter coefficients $\mathbf{w}$ per time step. It contains the cross-correlation vector of $\mathbf{x}(n)$ and $e(n)$. This means, the output $\hat{d}(n)$ of the adaptive filter contains the components of the error signal, which correlate with the input signal. During the calculation of the error signal, this component is subtracted from $d(n)$ (Fig. 2.6). Therefore the algorithm performs a successive decorrelation of input and error signal. The adaptation continues as long as there exists a correlation between the two signals.

In order to guarantee convergence, the parameter α needs to remain inside certain bounds given by relation 2.10.

$$0 < \alpha < \frac{2}{I\overline{x^2}} \tag{2.10}$$

This stability bound together with the definition of the normalized convergence coefficient $\tilde{\alpha}$ yields Equation 2.11. In reality $\overline{x^2}$ has to be estimated from previously measured data by averaging over the last I values, where I corresponds to the number of coefficients of the adaptive filter [20].

$$\alpha = \frac{\tilde{\alpha}}{I\overline{x^2}} \tag{2.11}$$

$$0 < \tilde{\alpha} < 2$$

2.2.3.5 The Filtered-Reference LMS Algorithm

Using the LMS algorithm presented in the previous section, the physical path between actuator and error sensor remains unconsidered. This can

lead to instability of the algorithm in the case of significant phase shifts along the secondary path. This can be prevented by using the filtered-x LMS algorithm instead. In Figure 2.7 the difference with regard to the LMS algorithm is illustrated.

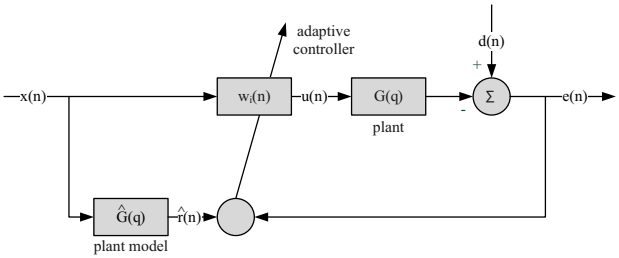

Figure 2.7: Block diagram of an filtered-x LMS algorithm [20].

Here the gradient of the cost function 2.12 together with $\mathbf{r} = \mathbf{x}G(q)$ results in Equation 2.13, with q being the forward shift operator.

$$e^2(n) = (d(n) - G(q)\mathbf{w}^T\mathbf{x}(n))^2 \tag{2.12}$$

$$\frac{\partial e^2(n)}{\partial \mathbf{w}} = -2e(n)\mathbf{r}(n) \tag{2.13}$$

Finally, this leads to the update relation 2.14. In the practical implementation the necessary reference signal $\mathbf{r}$ is generated by filtering $\mathbf{x}$ with a model of $G(q)$. This implies that bevor starting the adaptive control an identification of the secondary path $G(q)$ has to be performed.

$$\mathbf{w}(n+1) = \mathbf{w}(n) + \alpha\mathbf{r}(n)e(n) \tag{2.14}$$

The convergence criterion for the filtered-x algorithm is defined by equation 2.15, which is derived analogously to the convergence criterion for the LMS algorithm, as shown above [20, 28].

$$\alpha_{max} \approx \frac{2}{N\overline{r^2}} \tag{2.15}$$

3 Experimental Setups and Procedure

3.1 Experimental Setup (Facilities of Technische Universität Darmstadt)

3.1.1 Laminar Wing Glove

3.1.1.1 Design and Construction

In order to enable experiments under atmospheric conditions using DBD plasma actuators at Reynolds numbers relevant for small civil aircraft, a flight-capable testing platform has been constructed. The prominent feature of the laminar wing glove is its capability to be used in the low-speed wind tunnel facilities of the Technische Universität Darmstadt, as well as on a GROB G109b motor glider, which is stationed at the local airfield.

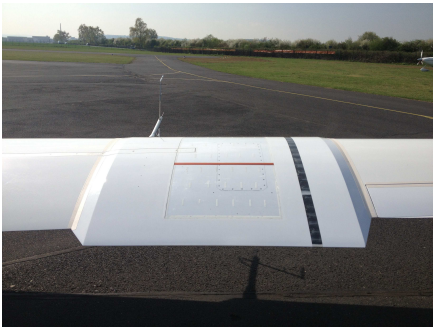

Figure 3.1: Laminar wing glove mounted on aircraft.

The wing glove design has been adopted from a research project investigating the influence of atmospheric turbulence on the performance of laminar airfoils. Therefore, only a brief summary of its aerodynamic characteristics is given here and the focus is on the adaptations that have been implemented for flow control purposes. For a detailed description of the design process the reader is referred to the work of Weissmüller [62].

The airfoil of the wing glove is based on a *DU84-158* profile, which is used on *ASW24* sailplanes. This laminar flow airfoil has been chosen because of its suitability for receptivity investigations, as well as for transition control experiments. The profile has been modified such that the pressure gradient on the pressure side of the airfoil can be adjusted from destabilizing, over approximately zero, to favorable pressure gradients depending on the operating conditions. These adjustments make the pressure side the preferred choice for transition control experiments. Furthermore, lift and drag have been adjusted to match the characteristics of the undisturbed wing section and to compensate for the additional weight and, thus to maintain the flight characteristics of the aircraft, despite of the asymmetric loading when the glove is installed.

Figure 3.2: Laminar wing glove mounted in the wind tunnel at the Technische Universität Darmstadt.

To establish an approximately two-dimensional flow field within the measurement area, a quadratic planform aligned in freestream direction has been decided on. A transition area of $0.1m$ width on each side matches the outer shape of the glove to the trapezoidal wing of the aircraft. Last but not least, a storage pod and a smaller covered compartment inside of the glove provide the necessary space to install the instrumentation.

The compartment inside of the glove is used to house two high-voltage generators (Minipuls 0.1, GBS Elektronik GmbH) during the flight experiments. This is advantageous, since this way the distance between the plasma actuators and these high-voltage generators is short and the equipment is spatially separated from the sensitive data acquisition sys-

tem, which is located in the underwing pod.

Numerical investigations [54] confirmed, that the assumption of two-dimensionality along the mid-section of the measurement area is valid for both sides of the airfoil and that the distortion of the flow field due to the storage pod is within acceptable limits. The overall dimensions of the wing glove are $1.35m \times 1.55m$ in streamwise and spanwise direction, respectively.

In order to use the wing glove in the Göttinger-type wind tunnel (NWK1) of the Technische Universität Darmstadt, a wing section of a Grob G109b aircraft has been prepared to fit the support of the tunnels force balance. The glove can be mounted in similar fashion as on the aircraft, only the orientation in the tunnel is vertical (Fig. 3.2).

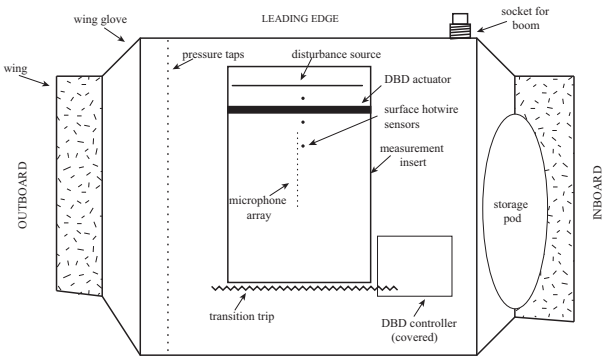

Figure 3.3: Schematic view on the pressure side of the laminar wing glove.

Figure 3.3 gives a schematic view of the pressure side of the laminar wing glove. The flow direction is from top to bottom. A flush-mounted inlay made of perspex (PMMA) material with a thickness of $1.5mm$ is fitted into the wing glove during the construction process. Its dimensions are $0.9m \times 0.6m$. It provides an exchangeable, non-conducting surface for the installation of actuators and sensors. Using an inlay, the setup is adaptable to different experimental requirements, without compromising the structural integrity of the carbon fiber composite material.

In addition to the plasma actuators, the instrumentation consists of a disturbance source, flush-mounted surface hot-wires, which are utilized as reference and error sensors for closed-loop control circuits, as well as a microphone array to determine the transition location during the in-flight

measurement campaigns. An aluminum boom is mounted on a socket inboard at the leading edge. A single hot wire is mounted on the tip of the boom in order to characterize the incoming flow. The boom also houses pressure ports to measure static and total pressure. In the outboard region of the wing glove, 64 pressure taps are embedded into the surface. The stainless-steel tubing connecting to the taps has been laminated into the composite material during the construction process. The pressure taps have a diameter of $0.2mm$. The spacing of the taps is variable, with a higher density at locations of large expected pressure gradients, like the leading edge area. The taps are used to monitor the pressure distribution around the airfoil during the transition control experiments. Downstream of the measurement region a transition trip is applied in order to force transition at a defined location for the uncontrolled cases. The components of the instrumentation are described in more detail in the following sections.

3.1.1.2 Disturbance Source

In order to generate boundary layer disturbances of defined characteristics, a disturbance source is integrated into the wing glove. The generated disturbances can be single frequencies or they can be composed of a mixed frequency content.

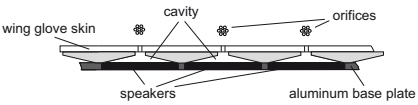

(a) Schematic view of the individual point sources with loudspeakers and orifices.

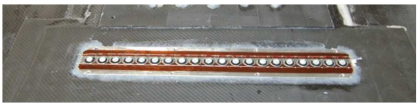

(b) Disturbance source integrated on the pressure side of the airfoil before joining top and bottom shell of the laminar wing glove.

Figure 3.4: Disturbance source for the laminar wing glove.

The disturbance source for the laminar wing glove had to fulfill several design criteria. First of all, the device had to be thin. A maximum thickness of $8mm$ was determined, since the spacing between wing and the glove is small near the leading edge. Additionally, the device had to be lightweight and able to excite broadband Tollmien-Schlichting waves, which could be pulsed with a short reaction time. For these reasons it was decided to

use a well proven concept (Fig. 3.4), which consists of a spanwise row of 20 point sources. Each point source is driven by a miniature loudspeaker (VISATON K-16), which modulates the pressure in a small cavity. The pressure fluctuation is then introduced into the boundary layer through a ring of six distributed delivery ports with a diameter of $D = 0.2mm$ each.

The velocity fluctuation generated at each point source is convected downstream and is spreading in the spanwise direction. In the case when all of the point sources are operated in phase, a quasi two-dimensional wave front forms. The spanwise uniformity of the phase and amplitude distribution has been investigated in the wind tunnel and was found to be sufficient for the intended experiments, as shown in section 4.2.2. This type of disturbance source was originally designed at the Technische Universität Berlin and has successfully been applied within the framework of several research studies [21, 45, 46].

3.1.1.3 Plasma Actuators

Plasma actuators have some apparent advantages for the use as flow control devices. For example their fast response time and their compact design. The absence of any moving parts also prevents unwanted vibrations of the aerodynamic surface, which could compromise the flow control results. For all experiments on the laminar wing glove the same type of plasma actuator is utilized.

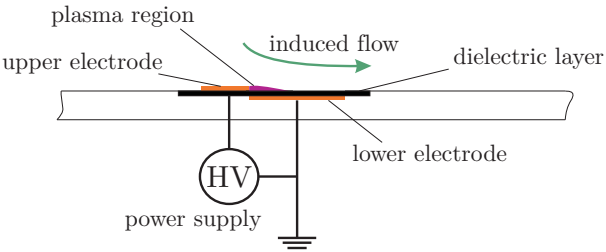

Figure 3.5: Cross-sectional view of the plasma actuator used for transition control experiments.

Figure 3.5 illustrates the layout of the DBD plasma actuator. The two asymmetrically placed copper electrodes consist of copper-tape with a thickness of $0.07mm$. They are mounted edge-to-edge without gap. The

streamwise width of the exposed electrode is $5mm$, the lower electrode has a width of $10mm$. The electrodes are separated by a layer of polyimide, which serves as dielectric material. The thickness of the dielectric material is $0.3mm$ resulting in a overall thickness of the actuators of approximately $0.4mm$. The lower electrode of the plasma actuator is insulated with an additional layer of dielectric material in order to prevent the formation of an unwanted secondary plasma discharge.

3.1.1.4 High-voltage Power Supplies (Minipuls 2.1/Minipuls 0.1)

Under laboratory conditions size and weight of high-voltage generators are usually of subordinate significance. Much more important is the quality of the output signal and the accessible output power. Popular devices are for example TREK amplifiers, like the $TREK30/20A$. They feature a high slew rate, high output power, but are large devices with a weight of approximately $70kg$. In view of in-flight experiments the high-voltage generators had to combine the properties of the laboratory devices as far as possible with low weight and compact design.

In close collaboration with GBS Elektronik GmbH a set of such high-voltage generators has been developed. For the wing glove experiments the Minipuls 2.1 (Fig. 3.6) is utilized for wind tunnel experiments, and the Minipuls 0.1 (Fig. 3.7) is employed for the in-flight investigations.

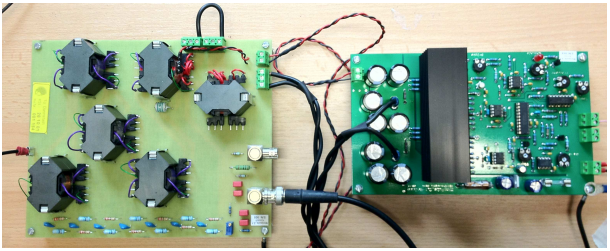

Figure 3.6: High-voltage power supply Minipuls 2.1 by GBS Elektronik. Signal generator (right) and transformer cascade (left).

Both devices consist of a signal generator and driver board and a transformer cascade amplifying the signal to the desired voltage suitable for a dielectric barrier discharge. The signal generator board autonomously generates the carrier signal for the plasma actuators. This is an important

feature in order to save computational power, which is primarily needed for the closed-loop control in active wave cancelation mode. A separate analog input signal in the range between $0V$ to $5V$ controls the amplitude modulation of the carrier signal. The wave form of the amplitude modulation can be prescribed arbitrarily by the control system, but is, of course, limited by the response time of the oscillatory circuit.

Such an analogue modulation feature allows for a precise adjustment of the amplitude of the body force produced by the plasma actuator at a very low response time. The transformer cascade is optimized to fit the capacitive load of the plasma actuators, since a suitable resonance frequency is of great importance for the accuracy of the modulation of the high voltage and therefore for the success of the transition control experiments. The operating frequency of the plasma actuator has to be located well outside of the unstable frequency band of the boundary layer such that fluid mechanically, a quasi-steady force production of the actuators can be assumed.

The Minipuls 0.1 is optimized for the in-flight application in terms of weight ($0.34kg$) and dimensions. It was originally designed to be used on unmanned aerial vehicles (UAV). As a compromise, the output power is limited to about $30W$ for this version.

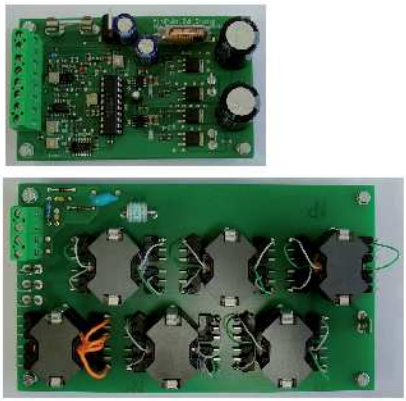

Figure 3.7: High-voltage power supply Minipuls 0.1 by GBS Elektronik. Signal generator and driver board (top); transformer cascade (bottom).

3.1.1.5 Sensors

An important task during the design process of the experimental setup is the implementation of suitable sensors for detecting the frequency and amplitude of the incoming boundary layer disturbances. They have to conform to largely conflicting specifications when used in combination with plasma actuators. The sensors have to be flush-mounted into the aerodynamic surface, such that the boundary layer downstream of their location is not disturbed and premature transition due surface imperfections is avoided. However, flush-mounting of the velocity sensors results in a low signal-to-noise ratio (SNR). At the same time, the sensors are mounted very close up- and downstream of the plasma actuator, which causes a high level of electromagnetic noise in the signal. To remedy these issue, the frequency of the plasma actuators carrier signal is removed by filtering, since this frequency is located outside of the fluid-mechanically relevant frequency band. Care has to be taken that the electromagnetic interference at TS frequency is low compared to the TS-wave signal. Otherwise the measurements can be compromised, since the signature of the interferences is of the same waveform and frequency as the TS-wave signal.

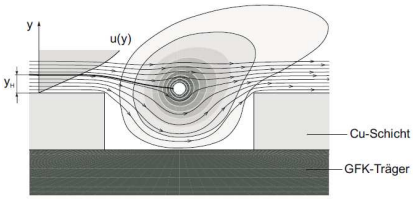

Figure 3.8: Schematic flow field around a surface hot-wire. (Source: Nitsche and Brunn [44])

Basically three different types of sensors have been investigated for the use on the laminar wing glove. The velocity fluctuations of a TS wave are coupled with corresponding pressure fluctuations, which can be detected at the wall. Therefore, the use of pressure sensitive piezo-electric sensors was considered initially.

The SNR ratio proved to be high enough to capture the TS-wave amplitude and phase angle, but at the same time the sensors exhibited a large susceptibility to electromagnetic interference. Additionally, the use of this type of sensor was not possible in the wind tunnel due to acoustic noise originating from the fan blades.

Similarly the use of hot-film probes has been considered. However, due to their working principle, the SNR is low. Secondly, due to the large surface area of the vapor-deposited electrodes they are highly susceptible to electromagnetic irradiation.

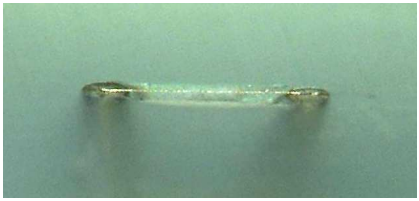

Figure 3.9: Surface hotwire for laminar wing glove.

A good compromise for this application are surface hot-wires (Fig. 3.8). Following the design of [11, 44] a hot wire is placed in spanwise direction over a rectangular microscopic channel. This channel serves two purposes. On the one hand, the hot wire becomes thermally insulated from the aerodynamic surface; and on the other hand, a minute deflection of the flow in direction of the cavity increases the SNR ratio significantly, as compared to a hot-film sensor. Figure 3.9 shows the prototype of the in-house manufactured surface hot-wires. The electrodes are cast into epoxy resin. The surface is machined such that the electrical contact points lay in-plane with the aerodynamic surface. The channel is machined manually with the use of a microscope. Gold-plated tungsten wire with a thickness of $5\mu m$ is used, which is of the same type used for commercially available CTA probes.

Downstream of the plasma actuators in the mid-section of the wing glove a streamwise array of microphones is installed in order to detect the transition location on the pressure side of the airfoil. This method is advantageous for in-flight experiments, since it is non-intrusive and delivers simultaneous measurements over the complete covered chord length. The array begins at a streamwise location of $x/c = 0.37$ and consists of 15 Sennheiser KE 4-211-2 microphones, which are mounted underneath the measurement inlay. Each microphone cavity is connected to the aerodynamic surface via an orifice with a diameter of $0.2mm$. The transition region can resolved with a spatial resolution of $30mm$, which is the inter-microphone spacing. The microphone signals are sampled at a frequency of $16kHz$ in order to avoid aliasing of the electromagnetic noise, induced by the plasma actuator, which were operated at a resonant frequency of $7.6kHz$ during the in-flight

experiments.

Stainless steel tubing is embedded in the wing glove shell during the construction process in order to provide 64 pressure ports at the outboard side of the measurement inlay. The ports, with a diameter of $D = 0.2mm$, are distributed along both sides of the airfoil to track the pressure distribution during the measurements. The spacing of the ports is variable with a higher density in regions of high pressure gradients.

3.1.2 In-Flight Measurement System

3.1.2.1 Motorized Glider GROB G109b

The Technische Universität Darmstadt owns two GROB G109b motorized gliders, which are stationed at the local airfield. One of the aircrafts is modified to be used as a platform for aerodynamic research. During this study no modification to the aircraft itself and the Dornier air-data system is done, therefore only a short description of the aircraft features is given in this section, summarizing the information given in [21] and [62].

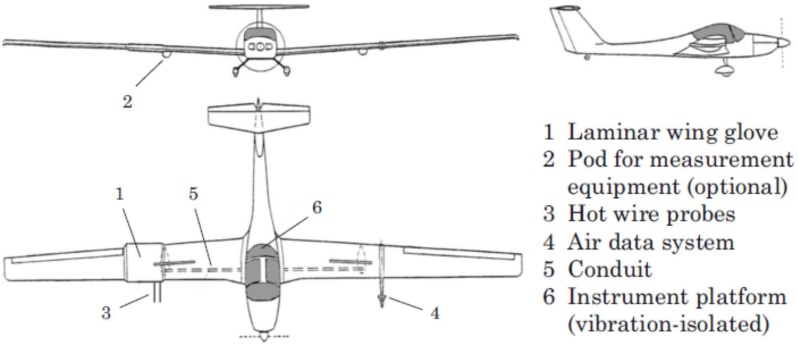

Figure 3.10: Schematic view of G109b aircraft and measurement equipment.

The airplane is a two-seater in side-by-side configuration, which is advantageous for the conduction of experiments, since pilot and experimentalist can communicate directly during the campaigns. The aircraft is self-launch capable and also performs well in gliding flight, for which the variable pitch propeller can be feathered. This provides a clean flow field on the wing

glove without structural vibration originating from a running engine or flow disturbances from the propeller wash.

Figure 3.10 gives an overview of the flight setup. The laminar wing glove (1) is mounted between airbrake and aileron on the right wing. The underwing pod (2) housing the data acquisition equipment is located on the inboard side. A boom (3) with hot-wire and pressure sensors is used to track the most important parameters of the incoming flow. On the left wing a Dornier Flight Log system (4) is installed, which is capable of measuring the attitude of the plane and gives environmental data as well. Cable ducts (5) connect wing glove and air data system to the fuselage, where an additional instrument platform (6) is located in the baggage compartment. Two displays are added to the cockpit, as shown in Figure 3.11. On the left side information on angle of attack and yaw angle is displayed to the pilot. On the right side the experimentalist runs the measurement via a computer screen.

Figure 3.11: Cockpit instrumentation of the GROB G109b aircraft.

3.1.2.2 In-Flight Data Acquisition System

Figure 3.12 shows all components of the measurement system in detail. The air data system on the left wing tracks the attitude of the plane and

the ambient flow conditions. Angle of attack and yaw angle are measured with a Dornier flight log system. Both variables are important to set and maintain the correct flow conditions on the wing glove and are therefore displayed to the pilot as crosshairs. Additionally, total and static pressure are sampled, as well as ambient temperature and humidity. The environmental data are sampled at a relatively low rate of $100Hz$, but are of great value as a redundant check on the validity of the data from the wing glove's sensors on the right wing. The temperature is sampled with a PT 1000 sensor, the sensors for static and dynamic pressure are a SETRA 270 and a SETRA 239 sensor, respectively. The digital conversion is done by a National Instruments NI6221 A/D board.

On the right side of Figure 3.12, the electrical setup of the wing glove is shown. This part of the setup is located in the underwing pod. For a detailed description of the actuators and sensors, see section 3.1.1. The data acquisition process is handled by a National Instruments CompactRIO RT-system (NI 9024). Several expansion input/output modules are necessary to acquire the data of all sensors simultaneously. Two NI 9205 analog input modules sample the data from the hot wire at the boom, the 3 surface hot wires, and the 15 channel microphone array at a sampling rate of $16kHz$. A NI9222 high-speed analog input module with simultaneous sampling of 4 channels is used to capture high-voltage and current at the plasma actuator at a rate of $100kHz$. This high sampling rate is necessary to resolve the individual discharge cycles with sufficient accuracy. The TTL carrier signal for the plasma actuator's operating frequency is generated by a NI9402 high-speed bi-directional digital input/output module.

Additionally, a CANDAQ unit in combination with a 64 channel pressure transducer (Pressure Systems ESP 64HD) samples the static pressure from the pressure ports used for tracking the pressure distribution around the airfoil. The disturbance source is operated by a handheld signal generator (Velleman HPG1) in combination with a small audio amplifier.

In the fuselage of the airplane, center section of Figure 3.12, two computers are located on a platform in the baggage compartment. The data acquisition system is operated from the right seat using National Instruments LabVIEW running on a fully equipped PC in compact design. This computer also processes the flight log data and displays the target angle of attack, as well as the yaw angle to the pilot. A dSPACE MicroAutoBox II runs the adaptive control algorithm used for active wave cancelation and hybrid mode. The compact real-time system is capable of running up to 3 controllers simultaneously. It processes the signals of the three surface hot-

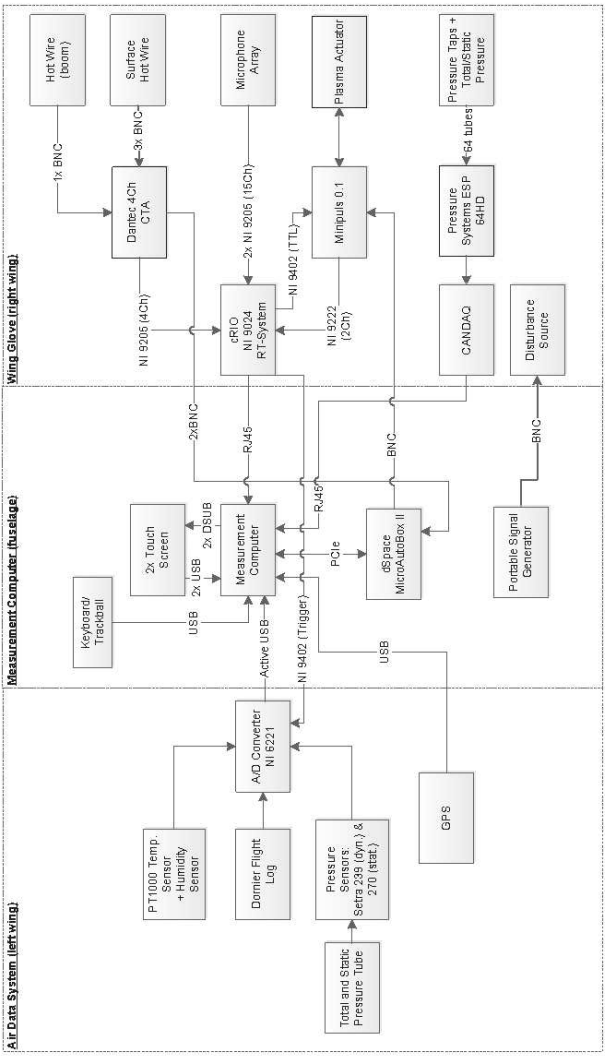

Figure 3.12: Data acquisition system for in-flight measurements.

wires and calculates the control signal, which is fed back to the high-voltage source of the plasma actuators.

3.1.2.3 In-Flight Measurement Procedure

The functionality of all actuators and sensors is tested on the ground before a scheduled take-off. During the climb of the aircraft to $10.000 ft$ maximum altitude, which takes about 20 to 30 minutes, the measurement equipment is run up and tested once again. This includes, for example, the functionality of the hot wires, the response of the microphone array, communication between data acquisition software and dSPACE system, as well as the high-voltage generators. When the maximum altitude is reached and the pilot begins the engine shutdown procedure and feathering of the propeller, the target conditions for the experiment are set.

Once a straight coordinated gliding flight is established, the pilot trims the aircraft on the target angle of attack. The disturbance source is set to the desired amplitude and the adaptive closed-loop controller together with the plasma actuators are started. The measurement time during each gliding flight is about 15 minutes, before another climb to $10,000 ft$ is necessary. For safety reasons, the gliding path is chosen such that a suitable landing site is at hand when the minimum allowed altitude is reached. The measurement equipment is partially switched off to save battery power and the next climb is initiated.

During an initial flight in clean configuration the microphone array has been calibrated. Due to fabrication tolerances of the microphones and the installation in the wing glove, their output level varies for the same pressure fluctuations. To compensate for this effect, a turbulence trip is installed upstream of the microphone array to trigger transition, such that all microphones are located in fully turbulent flow. The output level is then equalized with the first upstream microphone (reference) using scaling factors.

3.1.2.4 Time-Resolved Intermittency Factor

A typical method for the characterization of a transitional boundary layer is to acquire data at a certain wall normal position along the streamwise direction using a hot wire. For postprocessing purposes, the RMS value of the velocity fluctuations is plotted along the streamwise direction. This approach shows small RMS values for laminar flow, while the amplitude grows in the transitional region and finally settles on the turbulent level once the

transition process is completed. For the controlled, constant conditions present in a wind tunnel this approach is certainly valid. Nevertheless, analyzing in-flight transition control experiments, it is also of great interest to view the transition delay result over time, in order to judge the sensitivity towards turbulence or fluctuations in the angle of attack, as for example demonstrated in Reeh et al. [50].

Another approach relies on analyzing the frequency spectrum of the hot-wire data at each streamwise position and the flow is considered as turbulent once a broad spectrum of frequencies appears. This kind of measurements have also been performed by Duchmann et al. [19] using a traversable hot wire on the wing glove, but the method turned out to be too time consuming for in-flight experiments and the necessary traverse system can modify the flow field around the airfoil. Therefore, the current flight setup relies on surface mounted sensors, i.e. 15 wall microphones and three surface hot-wires, to evaluate the effectiveness of the control.

A quantity often used for transitional boundary layer characterization is the intermittency factor. The intermittency factor is a parameter describing the stage of the transition process in a laminar-turbulent boundary layer. It is defined as:

$$\gamma = 0(\text{for laminar flow}) \tag{3.1}$$

$$\gamma = 1(\text{for fully developed turbulent flow}) \tag{3.2}$$

$$0 < \gamma < 1(\text{for transitional flow}) \tag{3.3}$$

For the transitional region, there are several methods for the determination of γ. Zhang et al. [64] presents some common methods and compares them for different applications. In this study, the u-method is used, but since the laminar-turbulent transition is a dynamic process and the environmental conditions can vary during flight, an approach is needed in order to view the transition control effect over time. For this reason, the u-method is modified, such that time-resolved information about the intermittency factor can be extracted from the data.

Figure 3.13 shows a time trace of the voltage fluctuations of surface hotwire 3 at the transitional stage. In the left portion of the plot the fluctuations are small, whereas turbulent peaks start to occur more often in the section on the right.

In applying the u-method first, the data are averaged over a certain time interval, which is chosen to be $\Delta t_1 = 2 \cdot 10^{-2} s$ for all data sets. If a single data point within this interval exceeds the threshold (dashed line at

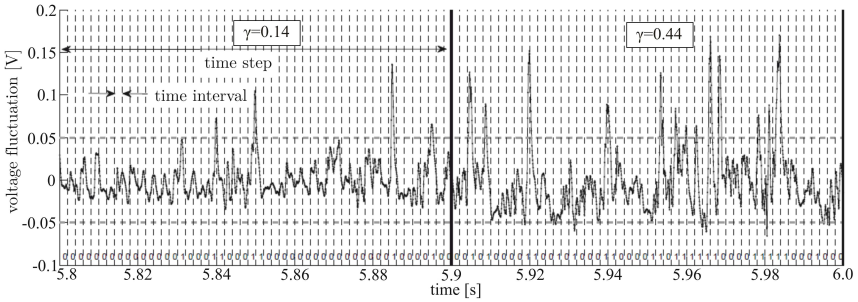

Figure 3.13: Determination of the time-dependent intermittency using surface hotwire data.

$V = \pm 0.05$) the whole time interval is considered turbulent and is marked with a "1". All other time intervals are considered laminar and therefore marked with a "0". Finally, the mean value of the time intervals is calculated with a time step of $\Delta t_2 = 0.1s$, yielding a value of $\gamma = 0.14$, and $\gamma = 0.44$ respectively, for the example in Figure 3.13. The time dependency of the intermittency factor can therefore be plotted with a temporal resolution of $0.1s$.

The critical part of calculating the intermittency is the selection of the threshold and the detector function. Fransson et al. [26] for example propose a method for the determination of the threshold with strict mathematical rules. Two major facts have to be taken into account when trying to apply these methods for the presented surface hot-wire signals. First, the measurements are taken directly at the wall where velocity fluctuations are not as distinct as at a wall-normal distance inside of the boundary layer, and secondly, the surface hot-wires are not calibrated in this case, while in the literature the threshold is usually set as a certain percentage of the mean flow velocity. Both issues require a manual determination of the threshold for the presented measurements. Time signals for known laminar and fully turbulent states are taken as reference. Using this procedure, the intermittency factor allows to quantify the progress of laminar-turbulent transition also with data of the uncalibrated surface hot-wire sensors. The time resolved approach provides information on the transition process over time, which is in particular important for in-flight experiments.

3.1.2.5 Time-Resolved Post-processing of Microphone Data

Similar to the postprocessing of the surface hot-wire signals, a time resolved analysis of the microphone signals is needed in order to evaluate the dynamics of the transition process. Since the microphones are located beneath the acrylic glass inlay and are only connected to the surface through a small orifice, the signal to noise ratio and the characteristics of the sensor signal do not allow the quantification of an intermittency factor. Furthermore, interferences occur at low frequencies, up to $1.2kHz$, and at the plasma operating frequency of $7.6kHz$, at times when the plasma actuator is operated. Unfortunately, these issue could not be resolved during the time given for the flight measurement campaign. As a possible workaround the signals are bandpass filtered from $f = 2.2 - 3.5kHz$. The result is a signal having a high level for turbulent flow, and a low level for laminar flow in this frequency band, which can be utilized to locate the transition region.

In order to view the transition location over time, the bandpass filtered microphone signals are subdivided into periods of $\Delta t = 0.1s$ duration, which is consistent with the temporal resolution of the intermittency factor in Section 3.1.2.4. The RMS value for each of the data packages is calculated and plotted as a contour plot over time. The result is a spatially and temporally resolved graph, showing the laminar and turbulent regions during a measurement. A comparison of both methods shows good agreement concerning the position of the laminar to turbulent transition.

3.2 Experimental Setup (Facilities of ONERA Toulouse)

3.2.1 Subsonic Wind Tunnel Facility and ONERA-D Wing Model

Within the framework of the European joint project PlasmAero, the possibility to run plasma actuators directly at the TS wave frequency has been investigated. The unsteady force production of a plasma actuator has been viewed as a problem for flow control purposes for a long time. This resulted also in a long-term discussion within the research community about the underlying mechanisms and the temporal distribution of the momentum generation within the discharge cycle. The idea behind the Direct Frequency Mode is to exploit the indisputable unsteady force production of the plasma actuator and take advantage of it. During the course of this

study, the feasibility of this approach has been investigated.

The presented experiments are conducted at one of the subsonic open-return wind tunnels located at the research facilities of ONERA in Toulouse. The open-return wind tunnel operates at ambient conditions. The turbulence level lies in the range of $0.5 \cdot 10^{-3} < Tu < 0.5 \cdot 10^{-2}$ depending on the free-stream velocity, which can be set from 5 to $75m/s$.

Figure 3.14(a) gives an overview of the setup in the wind tunnel. The two-dimensional model is mounted horizontally in the test section and can pivot around the vertical axis. The side-walls of the test section are sealed with adaptor-plates fitting the wing profile in the neutral position. To reduce vibrations of the model due to the large aspect ratio of the wing, adjustable supports on the side walls fix the model vertically, once the desired orientation is found.

The angle of attack can be adjusted between $\alpha = -8°$ and $\alpha = +3°$ in order to adapt the upper side pressure gradient and thus the natural transition location. For this experiment the angle of attack is set to $\alpha = 2°$ (Case 2: $\alpha = 1.5°$), which results in a natural transition located close to $x/c = 60\%$ for the given free-stream velocity of $U_\infty = 7m/s$ (Case 2: $U_\infty = 20m/s$). The setup also allows for an adjustment of the yaw angle (β), which is set to zero in this case. The airfoil has a chord length of $c = 0.35m$.

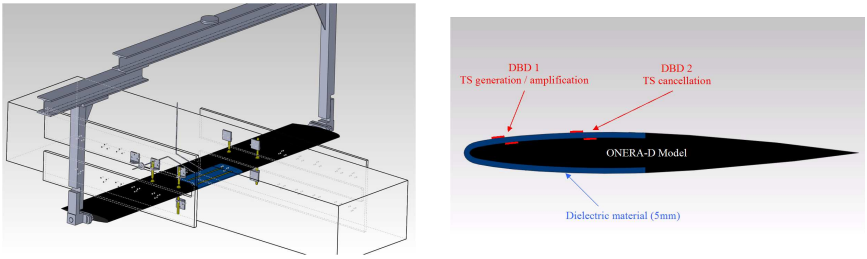

(a) Two-dimensional wing model of the ONERA-D airfoil mounted inside the wind tunnel.

(b) Cross-sectional view of ONERA-D wing model

Figure 3.14: Experimental setup for direct frequency mode experiments at ONERA (Toulouse).

A hollow insert is retro-fitted to the model in the center section to be equipped with plasma actuators. Figure 3.14(b) gives a cross-sectional view through the mid-section of the wind tunnel model. The ONERA-D profile

is symmetric and has been developed for transition control experiments. The insert at the leading edge area is made of dielectric material (Lab850) with a thickness of $5mm$, which is directly used as dielectric barrier for the plasma actuators. This allows for a free positioning of the plasma actuators in the nose area without further machining. Additionally, the wing is equipped with 15 pressure taps on the upper side to determine the pressure distribution.

3.2.2 Electrical Setup

As shown in Figure 3.14(b) two DBD plasma actuators are placed at 10% and at 30% chord, respectively. The upstream actuator (DBD1) serves as disturbance source to artificially excite a single frequency TS wave train. The plasma actuator downstream (DBD2) is utilized as transition control device. The DBD actuators used in this experiment consist of two thin $30cm$ long spanwise orientated rectangular electrodes made of copper tape. The electrodes are positioned asymmetrically on both sides of the dielectric insert. The two upper electrodes have been polished in order to reduce their thickness down to $0.05mm$ to prevent them from promoting transition.

Two TREK power amplifiers (model 30/20, $\pm 30kV$, $20mA$ peak) supply the power for the sinusoidally driven actuators. Two hot wire probes (Dantec, $55P15$) have been employed to analyze the flow downstream of the control actuator. One hot wire is mounted on a traverse system and serves for measuring boundary layer velocity profiles, whereas a stationary hot wire probe ($x/c = 40\%$, $y = 0.2mm$) is used as error sensor for the closed-loop control system. In-house LabVIEW codes at ONERA allow for automated hot wire calibration, as well as automatic traversing of the probe along the contour of the model. Filtering is applied online within the controller software in order to remove the electromagnetic noise emitted by the plasma actuators from the hot-wire signal.

4 Results of Wind Tunnel Experiments

4.1 Direct Frequency Mode Experiments (Facilities of ONERA Toulouse)

Historically, transition control using plasma actuators in wall-bounded flows can be subdivided into two groups. On the one hand, the plasma actuator can be operated in a continuous fashion, adding a quasi-steady momentum to the boundary layer close to the wall. It can be shown by linear stability analysis (LSA) that the modified boundary layer profile is stabilized. Locally the unstable frequency band of the boundary layer is narrowed or even suppressed for a certain downstream distance. Disturbances, which are already present in the flow, consequently decay, before the amplification process sets in again. This possibility has been investigated in several experimental studies, for example see [18, 33, 56]. On the other hand, authors use unsteadily operated actuators to act directly on the growing disturbances inside of the boundary layer, the so called Tollmien-Schlichting (TS) waves. TS-wave-induced transition is a common mechanism in two-dimensional flow at moderate Reynolds numbers [53]. In this case, the disturbance amplitude is reduced by negative superposition. The intention of this control mechanism is to remove the disturbances without changing the stability characteristics of the boundary layer. Using plasma actuators as a flow control device, this possibility was first investigated by Grundmann and Tropea [32].

At the same time experimental [24, 25] and numerical studies [8, 9, 58] investigated the underlying physical mechanisms responsible for the plasma actuators momentum generation. Even though it has been discussed controversially if the momentum generation is directed in the downstream direction during both discharge half-cycles ("push-push" and "push-pull" theories), it has been commonly accepted that the momentum production of a plasma actuator is in any case largely unsteady.

It is exactly this unsteady momentum production what makes the plasma actuator a candidate to be operated directly at the frequency of the Tollmien-Schlichting waves without the need of a amplitude modulation. Whereas

for a long time this unsteadiness in the momentum generation has been viewed as a problem regarding the plasma actuator's flow control application, it can also be exploited to ones advantage. The direct frequency mode offers the opportunity to increase the applicable Reynolds number range for active wave control using plasma actuators. This possibility was already suggested in [30] and has been realized for the first time during the course of this experimental study.

To demonstrate the feasibility of this approach, two cases have been investigated on the ONERA-D airfoil. This profile has been developed at ONERA (France) and is specifically designed for transition control experiments. Two measurement campaigns have been conducted. One set of experiments has been planned as a prove of concept at a relatively low Reynolds number based on chord of $Re = 1.63 \cdot 10^5$ and an angle of attack of $\alpha = 2.0°$ (case 1). In a second step the Reynolds number has been increased to control TS waves at a higher frequency in the order of $1kHz$. Here the Reynolds number was $4.66 \cdot 10^5$ at an angle of attack of $\alpha = 1.5°$ (case 2).

4.1.1 Numerical Base Flow Analysis (Case 1)

Boundary layer calculations and linear stability analyses have been performed for both operating conditions in order to predict and confirm the experimental findings. The numerical results shown in sections 4.1.1 and 4.1.3 have been performed by O. Vermeersch at ONERA Toulouse.

In Figure 4.1 the dimensionless velocity distribution $U/U_\infty = (1-C_p)^{0.5}$ is plotted for an angle of attack of $\alpha = 2.0°$ and a Reynolds number of $Re = 1.63 \cdot 10^5$. The experimentally obtained data (□) has been smoothed by interpolation in order to provide a more refined external velocity distribution needed for the computational analysis. A well pronounced suction peak is visible followed by a strong deceleration region, which is promoting the amplification of unstable TS modes.

Figure 4.2(a) illustrates the resulting integral boundary layer parameters on the upper side of the profile. The computations have been carried out using the boundary layer code $3C3D$ [49]. Due to the strong adverse pressure gradient, the displacement thickness δ_1 experiences a large increase. Additionally, the momentum thickness δ_2 is growing, which consequently result in a relatively high shape factor H_{12}. The shape factor reaches a maximum value of $H_{12} \approx 3.5$ close to the leading edge. The simulation has been carried out until $x/c = 0.6$ where separation occurs. In Figure 4.2(b) experimentally obtained boundary layer profiles are compared to the

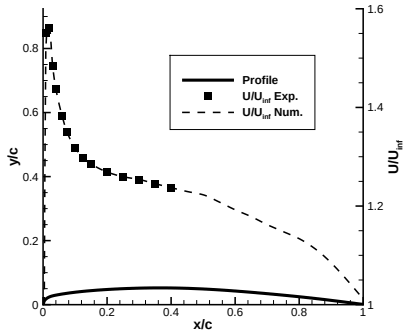

Figure 4.1: Dimensionless external velocity distribution along the ONERA-D airfoil for $Re = 1.63 \cdot 10^5$ and $\alpha = 2.0°$. Numerical results by O. Vermeersch (ONERA).

simulation. The profiles have been obtained at $x/c = 0.3$ and $x/c = 0.55$ using a traversed hotwire. Even though there is some deviation close to the separation location, the agreement between experimentally obtained data and the numerical prediction is rather good.

To describe the laminar-turbulent transition, it is common practice to distinguish three successive processes. The first, taking place close to the leading edge, is the receptivity. It describes the means by which external disturbances (such as free-stream turbulence or noise as well as wall surface imperfections) excite the eigenmodes of the boundary layer. In the following amplification phase, these eigenmodes develop into periodic waves which are convected in the streamwise direction. Some of them are linearly amplified and will trigger transition further downstream. Their evolution is well described by the linear stability theory. Once the amplitude of the waves is large, non-linear interactions occur and rapidly lead to turbulence (third step). In the framework of classical linear stability theory, disturbances are introduced as:

$$q'(x, y, z, t) = \hat{q}(y) \cdot e^{(-\alpha_i x)} \cdot e^{i(\alpha_r x + \beta z - \omega t)} \tag{4.1}$$

where q' is a fluctuation (velocity, pressure or temperature) and $\hat{q}$ its amplitude function (x is defined perpendicular to the leading edge and y normal to the wall). Considering the spatial theory, $\alpha = \alpha_r + i\alpha_i$ is

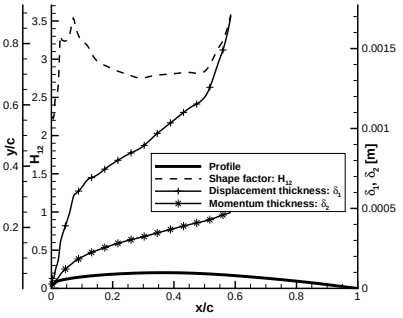

(a) Streamwise evolution of boundary layer displacement δ_1 and momentum thickness δ_2, as well as shape factor H_{12}.

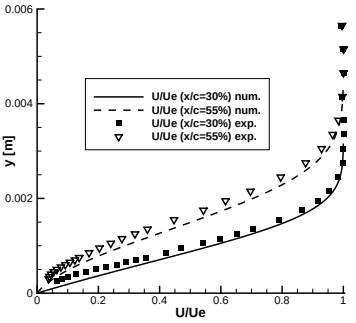

(b) Boundary layer longitudinal mean velocity profile at 30% and 55% of chord. Symbols stand for measurements, lines for numerical results.

Figure 4.2: Boundary layer integral parameters and boundary layer profiles at $Re = 1.63 \cdot 10^5$. Numerical results by O. Vermeersch (ONERA).

the complex wave-number in the x-direction. The spanwise wave-number β and frequency ω are real. Introducing expression 4.1 in the Navier-Stokes equations leads to a system of ordinary differential equations for the amplitude functions. The stability of the flow depends on the value of the imaginary part of the longitudinal component of the amplification vector α_i. When α_i is positive, the flow will be stable, when it is negative, the perturbation will be amplified and transition will be triggered.

To quantify the amplification of disturbances, the so-called N factor given by relation 4.2 is introduced.

$$N = \ln(\frac{A}{A_0}) = \int_{x_0}^{x} -\alpha_i(\xi)\,\mathrm{d}\xi, \tag{4.2}$$

where A is the amplitude of the disturbance at a streamwise position x. Physically, the N-factor describes the total amplification rate of small disturbances along the propagation path. Considering low velocity two-dimensional flow, only two-dimensional waves ($\beta = 0$) need to be considered, since Squire's theorem states that they are the most relevant ones. The N-factor is computed by integrating $-\alpha_i$ in streamwise direction.

The stability calculations have been performed using the numerical code CASTET [48]. Figure 4.3 represents the linear stability computation on the upper side of the ONERA-D airfoil for an angle of attack of $\alpha = 2.0°$ and a Reynolds number based on chord of $Re = 1.63 \cdot 10^5$ (case 1). A first analysis has been undertaken for frequencies between $0.2kHz < f < 1kHz$ in steps of $\Delta f = 0.2kHz$ (Fig. 4.3(a)). As the frequency increases, the maximum of amplification is reduced and moves towards the leading edge. After narrowing down the unstable frequency band, the computation has been repeated with higher resolution, $200Hz < f < 400Hz$ with $\Delta f = 40Hz$, corresponding to the order of magnitude of the plasma actuation frequency. The results are presented in Figure 4.3(b). At $x/c = 0.3$, the location of DBD2, the most unstable frequency is in the range of $f = 280 - 320Hz$. In general, the numerical findings obtained with the linear stability analysis agree well with the experimental observations.

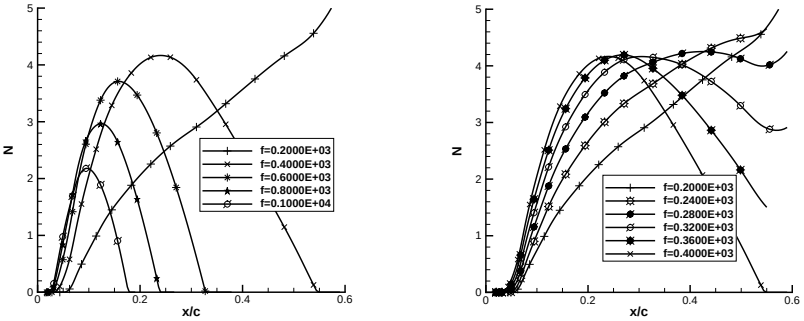

Figure 4.3: Linear stability analysis for case 1 ($Re = 1.63 \cdot 10^5$, $\alpha = 2.0°$). Numerical results by O. Vermeersch (ONERA).

4.1.2 Transition Control Results (Case 1)

The experiments have been split into two phases. During an initial testing phase experience had to be gained performing active wave cancelation on the ONERA-D wing model, as well as to use an additional plasma actuator as an artificial disturbance source on this airfoil. Following this step, the feasibility of the direct frequency mode for active wave cancelation using

a single DBD plasma actuator had to be proven. In order to do so, a setup employing a beat frequency approach without the use of a closed-loop controller was chosen, reproducing the experiments of Grundmann and Tropea [32]. This allows for time efficient parameter studies to find appropriate settings and the corresponding attenuation rates. In the second testing phase transition delay on the wing model has been demonstrated with closed-loop control applied, which is presented here. For the direct frequency mode experiments a extremum seeking approach as described in section 2.2.2 is applied. The perturbation for the estimation of the gradient is set to a period of $T = 1s$. The extremum seeking control is characterized by its robustness and performs well in this environment. The phase relation between actuation and the TS waves within the boundary layer is the optimized parameter since it is the most sensitive.

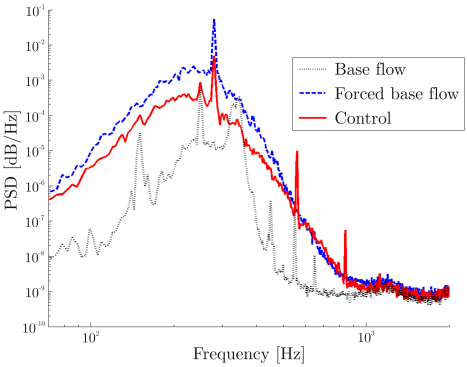

Figure 4.4: Spectral analysis of the error sensor signal at $x/c = 0.4$ for base flow, forced transition and controlled case at $Re = 1.63 \cdot 10^5$ and $\alpha = 2.0°$ (case 1).

Two plasma actuators have been used during this study. One of them serves as a disturbance source to create two-dimensional Tollmien-Schlichting waves. It is located at $x/c = 0.1$. The controlling plasma actuator is positioned at $x/c = 0.3$. A spectral analysis $35mm$ downstream of DBD2 at $x/c = 40\%$ reveals the frequency content of the flow, as shown in Figure 4.4. The signal of the error sensor of the closed-loop control system is used for this analysis. Plotted is the power spectral density in dB/Hz over frequency at a wall-normal position of $y = 0.2mm$. In the base flow case

(DBD1 off, DBD2 off) two frequency peaks, one at $250Hz$ and a wider peak around $340Hz$, are prominent. These frequencies represent the naturally occurring TS waves present in the boundary layer for the given flow situation. However, as had been shown with linear stability analysis, frequencies around $340Hz$ are damped downstream of DBD2, with the limit for the unstable frequency band being about $300Hz$. A frequency sweep in the unstable range revealed that an excitation at $280Hz$ is the most efficient, requiring only a low excitation amplitude at DBD 1. Consequently it was decided to use this frequency for the subsequent AWC experiments. Figure 4.4 shows that introducing the excitation at $x/c = 0.1$ (DBD1 on, DBD2 off) produces the expected peak around $280Hz$ as well as an overall increase in the turbulence level as transition is being promoted. This increase is visible at the error sensor, since its location is close to the transition region for the excited case ($x/c \approx 0.47$). Applying the control (DBD1 on, DBD2 on) the TS peak at $280Hz$ can be reduced by about one order of magnitude. This effect is accompanied by a decrease in the overall turbulence level.

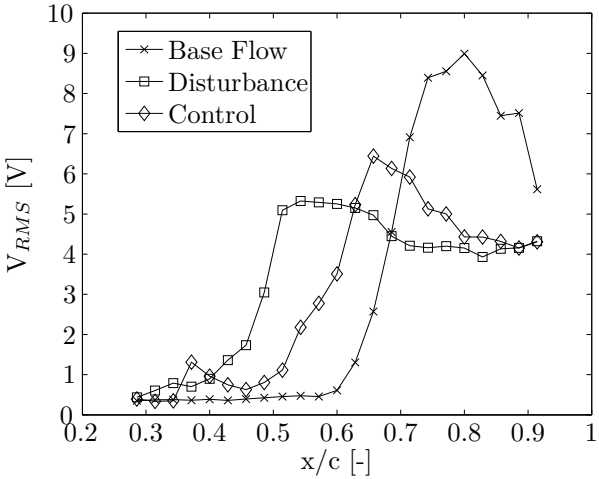

Figure 4.5: Transition positions for base flow, forced transition and control at $Re = 1.63 \cdot 10^5$ and $\alpha = 2.0°$ (case 1).

Figure 4.5 depicts a typical result of the transition delay studies. Plotted is the RMS value of the longitudinal velocity fluctuations recorded at various downstream locations at a constant distance above the wall within the boundary layer. It is well known that transition is characterized by

an abrupt increase of velocity fluctuations [53] due to the at first intermittent spots and then continuous presence of turbulent flow. In the natural transition case (×) the onset of transition is located at about 60% chord, i.e. neither the disturbance source nor the control actuator are operating. Running the disturbance source, the TS wave amplitude is significantly increased at $f = 280Hz$, which moves the transition region upstream to about 40% chord (□). With the control system active, the region of transition can be shifted downstream significantly by about 10% of chord.

Even though the unsteadiness of the force production of DBD plasma actuators is exploited in this work to conduct active wave cancelation it may not be neglected that also in this case a net force is produced, which modifies the mean flow, i.e. the stability characteristics of the boundary layer. This modification can by itself lead to a stabilization of the boundary layer and hence delay transition [33, 56]. Complementary measurements have been carried out in order to exclude a possible boundary layer stabilization due to continuous momentum addition. To quantify this effect, the momentum generation of DBD2 has been measured in quiescent air using pitot-tube measurements. The maximum achievable velocity, $10mm$ downstream of the active electrode, was determined to be $U \approx 0.6m/s$ at the prescribed plasma frequency of $280Hz$ using this electrode configuration, dielectric material and thickness. In order to deactivate the active wave cancelation and to quantify the effect of a pure momentum addition of this magnitude, the recorded average wall-jet velocity has been reproduced at a plasma frequency of 1kHz using DBD2. This frequency is located well outside the unstable frequency range and is assumed not to have any destabilizing effect on the boundary layer. The transition delay due to continuous momentum addition is small as compared to the effect of the active wave cancelation and is in the order of $1 - 2\%$ of chord length. For higher Reynolds numbers it can be assumed that this effect will be reduced even further. The experiment proves that the achieved results can clearly be attributed to the unsteady force production of the DBD plasma actuator and are not the result of a modified mean flow.

4.1.3 Numerical Base Flow Analysis (Case 2)

Following the successful proof of concept, a second measurement campaign has been planned. During this study the Reynolds number has been increased in order to show the potential of the direct frequency approach. The flow conditions for case 2 have been chosen to a Reynolds number of $Re = 4.66 \cdot 10^5$ and an angle of attack of $\alpha = 1.5°$. Also for this flow con-

ditions a boundary layer calculation and a linear stability analysis for the base flow case have been provided by O. Vermeersch at ONERA Toulouse. The boundary layer computations have been carried out using $3C3D$ [49] and the stability analysis is done using the numerical code CASTET [48].

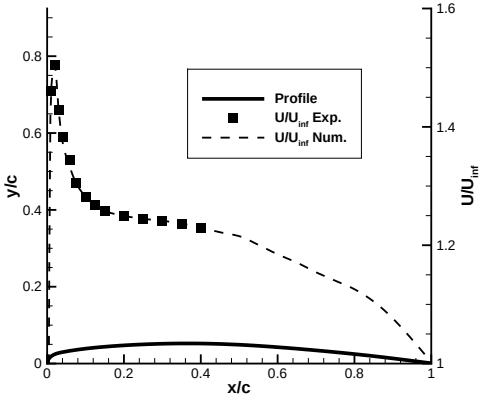

Figure 4.6: Dimensionless external velocity distribution along the ONERA-D airfoil for $Re = 4.66 \cdot 10^5$ and $\alpha = 1.5°$. Numerical results by O. Vermeersch (ONERA).

In Figure 4.6 the external velocity distribution is shown in a similar fashion as for case 1 in the previous section. A well pronounced suction peak is visible close to the leading edge of the airfoil. The external velocity reaches values of $U/U_{inf} \approx 1.5$. By reducing the angle of attack to $\alpha = 1.5°$ as compared to case 1, the strength of the suction peak has been reduced, which leads to a comparable external velocity distribution along chord. The suction peak is followed by a deceleration region promoting the amplification of Tollmien-Schlichting modes. The experimentally obtained velocity distribution is smoothed by interpolation. This allows to extract a more refined distribution as input for the numerical calculations.

The development of the integral boundary layer parameters is given in Figure 4.7. Similar to case 1, the displacement thickness δ_1 is growing strongly due to the adverse pressure gradient (Fig. 4.7(a)). This is accompanied with a growth of the momentum thickness δ_2. Both result in a high shape factor H_{12} close to leading edge of the airfoil reaching values of

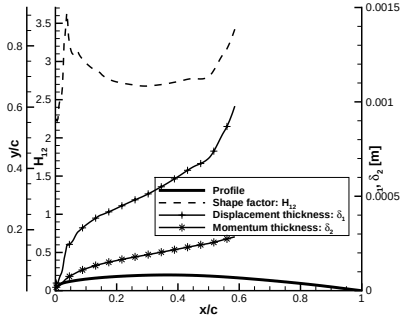

(a) Streamwise evolution of boundary layer displacement δ_1 and momentum thickness δ_2, as well as shape factor H_{12}.

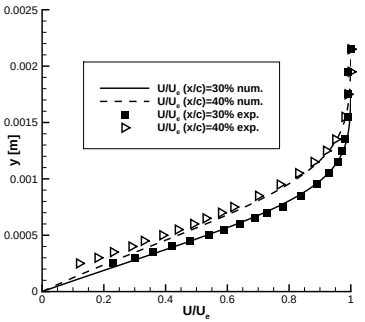

(b) Boundary layer longitudinal mean velocity profile at 30% and 40% of chord. Symbols stand for measurements and lines for numerical results.

Figure 4.7: Boundary layer integral parameters and profiles at $Re = 4.66 \cdot 10^5$. Numerical results by O. Vermeersch (ONERA).

$H_{12} \approx 3.6$, which is only slightly higher than for case 1 at reduced Reynolds number.

Two experimentally obtained boundary layer profiles taken at $x/c = 0.3$ and $x/c = 0.4$ are compared to the prediction of the numerical simulation (Fig. 4.7(b)). For case 2 the Reynolds number has been increased and the angle of attack reduced, which results in a comparable distribution of the external velocity, but to a reduced tendency towards flow separation in the deceleration region of the airfoil. If not fully prevented, the separation line moves downstream at the minimum. This can be observed in the prediction of the boundary layer profiles as well, where an improved agreement between experimentally obtained data and numerical results is visible.

The results of the boundary layer calculations are used as input for stability investigations. Figure 4.8(a) illustrates a frequency sweep in the range from $0.5kHz < f < 3.0kHz$ in steps of $\Delta f = 0.5kHz$. This sweep shows that the unstable frequency band has to be found around a frequency of $f = 1.0kHz$. Frequencies below this value are not amplified sufficiently until the trailing edge of the airfoil is reached, like in the case of the included curve for $f = 0.5kHz$. Frequencies above $1.0kHz$ are amplified in a region close to the leading edge, but are damped strongly further downstream

before they can trigger a laminar-turbulent transition. Additionally, with increasing frequency the maximum of the N-factor reduces and moves closer to the leading edge.

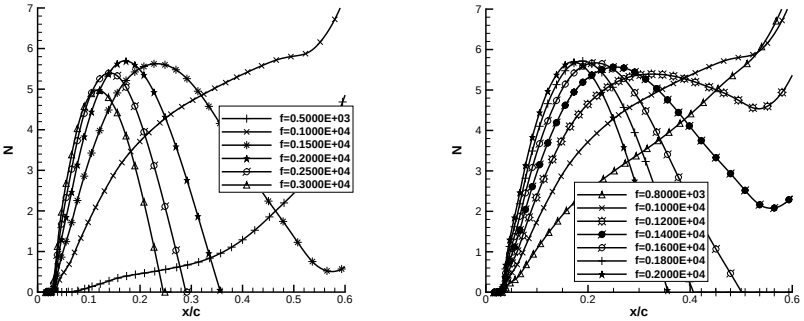

Figure 4.8: Linear stability analysis for case 2 ($Re = 4.66 \cdot 10^5$, $\alpha = 1.5°$). Numerical results by O. Vermeersch (ONERA).

The result of the frequency sweep has been used to narrow down the unstable frequency range for case 2. The refined analysis is shown in Figure 4.8(b). The frequency range is $0.8kHz < f < 2.0kHz$ in steps of $\Delta f = 0.2kHz$. Frequencies between $0.8kHz < f < 1.0kHz$ are unstable, whereas $f = 1.2kHz$ is already too high in order to reach an N-factor leading to transition before the trailing edge of the airfoil is reached. A parameter study varying amplitude and frequency of DBD1, which is used as a disturbance source, showed that forcing the flow with a frequency of $f = 1.0kHz$ is the most effective. At this frequency only a low amplitude is needed at the plasma actuator to induce a TS wave train with a clean signal in the region, where active flow control is applied.

4.1.4 Transition Control Results (Case 2)

With the determined settings a transition control experiment has been performed. In Figure 4.9 the results of this experiments are summarized. Also in this case extremum seeking control as outlined in section 2.2.2 is utilized. For the base flow case, the transition region begins at a streamwise location of about $x/c \approx 0.57$. For the case with forced transition, with the

upstream plasma actuator operating, the transition region moves forward to $x/c \approx 0.47$. Applying the control at the prescribed TS frequency of $f_{TS} = 1.0kHz$, the transition region can be shifted downstream to $x/c \approx 0.51$, and therefore a transition delay of $x/c = 4\%$ could be obtained.

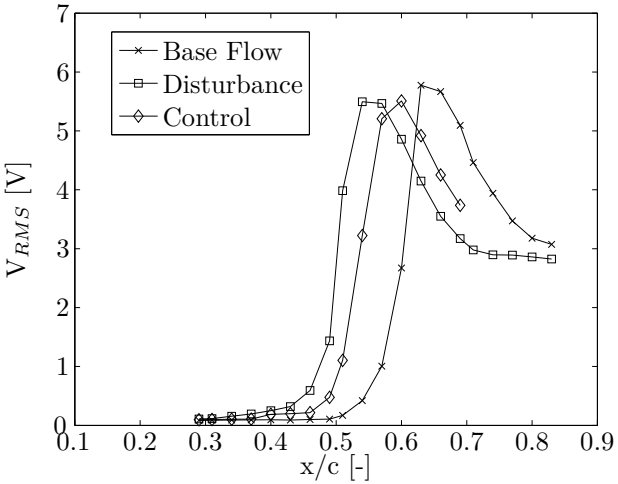

Figure 4.9: Transition delay at $Re = 4.66 \cdot 10^5$ and an angle of attack of $\alpha = 1.5°$. RMS values of traversed hotwire signal.

4.1.5 Phase-Locked Hotwire Measurements (Case 2)

Additionally to the traversed hotwire measurements, the boundary layer has been investigated further in order to prove two points. First of all, it had to be checked if the plasma actuator at $x/c = 0.1$, which served as Tollmien-Schlichting waves generator, has indeed excited TS waves and not only velocity disturbances of some sort. Therefore, the eigenfunction of the boundary layer disturbances had to be determined. And secondly, it is of interest to investigate the distribution of the damping result in the wall-normal direction. A uniform damping rate in the wall-normal direction is desired.

Due to the low amplitude of the disturbances a phase-locked hotwire technique is employed in order to extract the periodic signal of the disturbances out of the noise present in the boundary layer. The boundary layer velocity is measured over $t = 10s$ for each wall-normal position to resolve

the complete boundary layer at each downstream location. The spacing in wall-normal direction is variable with a high resolution close to the wall and a continuously lower density towards the boundary layer limit, where the gradients are smaller. Simultaneously to the hotwire signal, the excitation signal for the disturbances is recorded. During the post-processing an averaged disturbance signal can be reconstructed over one forcing period for each wall-normal position.

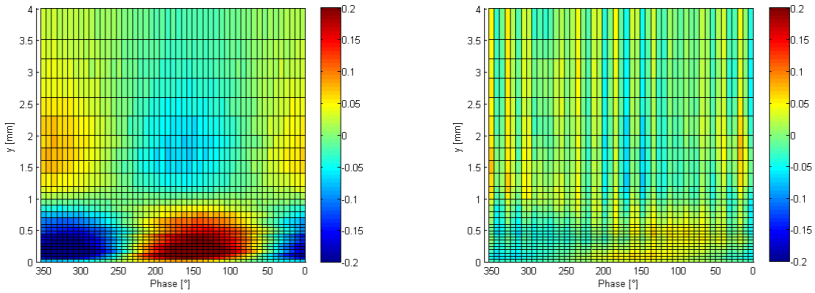

Figure 4.10: Phase-averaged disturbance signal over one forcing period for $Re = 4.66 \cdot 10^5$. Shown is the forced base flow and the controlled case.

Figure 4.10 illustrates the results of this measurement for the case 2 at a Reynolds number of $Re = 4.66 \cdot 10^5$ and an angle of attack of $\alpha = 1.5°$. The boundary layer data has been recorded at a downstream location of $x/c = 0.4$, $35mm$ downstream of the controlling plasma actuator. In the base flow case with applied forcing of DBD1 (Fig. 4.10(a)), the disturbance velocities are plotted. They are marked in blue for velocities lower than the local average velocity and in red for zones with velocities exceeding the average for the respective wall-normal position. Inside of the boundary layer a sinusoidal disturbance is traveling downstream with an amplitude of $U = \pm 0.2m/s$. At the boundary layer limit, which has a thickness of $\delta_{99} \approx 1.0mm$ in this case, the amplitude is close to zero. This is followed by a second, lower disturbance maximum outside of the boundary layer, which reveals a phase shift of $\Phi = 180°$, which is typical for a Tollmien-Schlichting wave. This shows that the disturbances generated using DBD 1 develop into a two-dimensional TS wave train with the typical footprint of the TS eigenmode.

Figure 4.10(b) shows the same measurement for the controlled case. The scaling is chosen similar to the case of forced base flow. The amplitudes of the TS wave are reduced by approximately 75%, in accordance with the observed transition delay. Even though the controlling plasma actuator induces velocities close to the wall, the disturbance signal outside of the boundary layer is reduced as well, indicating an even damping over the wall-normal direction, as desired.

4.2 Wing Glove Experiments (Facilities of Technische Universität Darmstadt)

Parallel to the direct frequency mode experiments the goal of active flow control in transitional boundary layers containing TS waves of mixed frequency content and amplitude has been persued at the Technische Universität Darmstadt. Several subsequent wind tunnel measurement campaigns using the newly built laminar wing glove setup have been carried out. These experiments served several purposes. In a first step, basic studies investigated the flow conditions around the airfoil. Operating points have been determined, where Tollmien-Schlichting waves occur on suction and pressure side of the airfoil and it was investigated how their occurrence and the position of the transition region can be influenced. Whereas under wind tunnel conditions angle of attack and Reynolds number can be adjusted independent of each other, they are coupled during coordinated and level flight. For this reason also operating points inside of the flight envelope of the GROB G109b aircraft have been investigated. This first set of experiments included the commissioning of the disturbance source as well. This device was newly designed with later in-flight experiments in mind and questions had to be answered, like can two-dimensional Tollmien-Schlichting waves be excited at all or is phase relation and amplitude from the single point sources sufficient. Disturbance introduction to a laminar boundary can be a delicate task. Many times problems with early transition occur due to bypass, or the two-dimensionality of the excited wave trains is not satisfactory.

In close collaboration with the Technische Universität Berlin two types of control algorithms have been implemented in a dSPACE real-time environment. A minimum seeking controller has been programmed, which is very robust and well suited for the control of single-frequency disturbances, and also an adaptive controller, which is capable of damping disturbances

of mixed frequency content. Both controllers have proven their capabilities during experimental studies at the Technische Universität Berlin and have been provided and modified for this study. However, they have been used with very different actuator concepts before and their function in combination with plasma actuators, as well as the linearity of its behavior was unknown.

Different sensors have been investigated in combination with the new control system to be used as reference and error sensors for the adaptive control. In the beginning, the use of hotfilm sensors or piezo-resistive pressure sensors has been investigated. Unfortunately, both types turned out to be unfeasible for the use in combination with plasma actuators due to problems with electromagnetic interference. Therefore, it was decided to rely on inhouse designed surface hotwires for the planned experiments. This process is described in more detail in section 3.1.1.5.

At a later stage, the disturbance input, even though still two-dimensional, has been varied in order to investigate the response of the adaptive control system to a mixed frequency input or a pulsing of the disturbances. This has been done in preparation of the control of naturally occurring TS waves, which will be subject of future projects.

After promising results in the wind tunnel a flight measurement setup was designed and built. This required a complete redesign and miniaturization of the components in the measurement system to fit the setup into the GROB aircraft. Thorough testing of all components has been done in order to assure fast and reliable data acquisition in flight. The results of the various wind tunnel experiments are presented in the following sections.

4.2.1 Base Flow Investigation

The wind tunnel experiments have been conducted at the closed-loop wind tunnel facilities (NWK1) at the Technische Universität Darmstadt. A base flow investigation has been conducted for the operating point at a Reynolds number based on chord of $Re = 1.41 \cdot 10^6$ and the angle of attack of $\alpha = 1.0°$. Reynolds number and angle of attack have been chosen such that transition for base flow, forced base flow and the controlled cases occurs within range of the installed sensor system and at a position suitable for the plasma actuators. Figure 4.11 illustrates the measured and the calculated C_p-distribution of the airfoil using Xfoil. In addition, the positions of actuators and sensors are given together with the LSA result for a frequency of $f = 120Hz$.

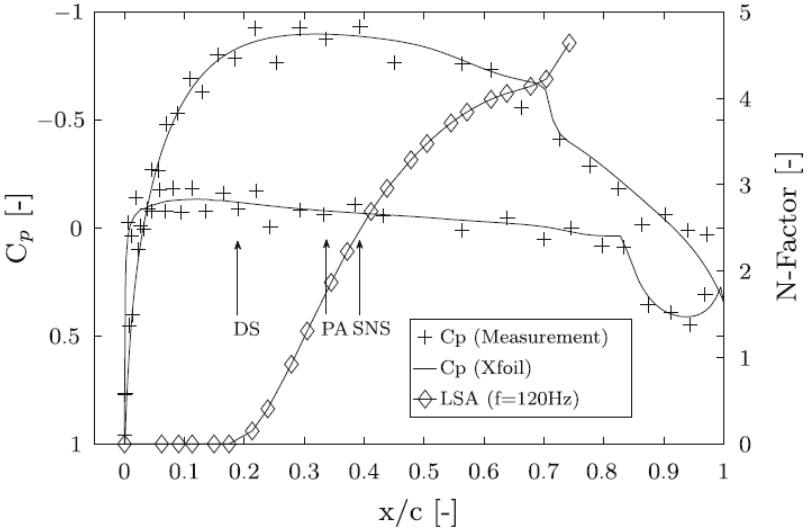

Figure 4.11: Measurement (+) and Xfoil calculation (solid line) of the airfoils pressure distribution at $Re = 1.41 \cdot 10^6$ and $\alpha = 1.0°$. Linear stability analysis for a frequency of $f = 120Hz$ ($\diamond$).(DS: disturbance source, PA: plasma actuator, SNS: surface hotwire)

As described in section 3.1.1, it has been decided to conduct the transition control experiments on the pressure side of the airfoil. On this side of the airfoil the pressure gradient can be varied from favorable, over approximately zero, to a destabilizing gradient depending on the operating conditions. As can be seen in Figure 4.11, the pressure gradient is almost linear and slightly destabilizing ($11Pa/m$)over a wide chord range promoting the growth of Tollmien-Schlichting waves in the boundary layer for this angle of attack. The C_p-distribution of the suction side of the airfoil reveals a smooth decrease without a strong suction peak, which is intended and typical for laminar airfoils. The plateau at a chordwise location of about $x/c = 0.7$ indicates a small separation bubble on the suction side for the relatively low Reynolds number. For providing controlled experimental conditions, the TS waves have been introduced artificially into the boundary layer. For this purpose, the wing glove is equipped with a disturbance source (DS) located at $x/c = 0.189$. It consists of a spanwise-oriented line

of point sources with a spacing of $\Delta z = 20mm$, which are driven in phase by miniature loudspeakers to create a two-dimensional wave front.

The controlling plasma actuator (PA) at $x/c = 0.337$ is composed of two copper tape electrodes separated by a layer of polyimide, which serves as the dielectric material. A flush-mounted surface hot wire (SNS) is utilized as error sensor for the control system $x/c = 0.392$ in this case. It captures the near-wall velocity fluctuations, which are correlated with the amplitude of the incoming TS waves. The maximum amplitude of the TS waves, normalized with the freestream velocity at the sensor location, was $A_{TS} = 1.31\%$. The characteristic eigenfunction of TS waves could be confirmed using a phase-averaged hotwire technique.

A linear stability analysis of this base flow case revealed that an appropriate frequency for the forcing of the flow is at a frequency of $f = 120Hz$. It is the most unstable frequency at the position of the controlling plasma actuator. The N-factor evolution for this frequency along chord ($\diamond$) shows a naturally occurring transition at $x/c \approx 0.75$. It confirms that this frequency remains unstable over the complete measurement range. Depending on the initial amplitude, that is applied at the disturbance source, transition can also positioned further upstream of this location.

4.2.2 Disturbance Source Characteristics

As part of the base flow experiments, the two-dimensionality of the TS wave train generated by the disturbance source has been investigated. It is of importance to the success of the transition control results that the amplitude, as well as the phase relation of all point sources is uniform in the spanwise direction.

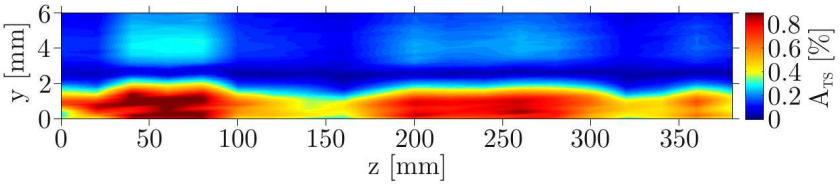

Figure 4.12: Spanwise amplitude distribution of incoming TS wave front.

In Figure 4.12 the amplitude of the Tollmien-Schlichting waves generated by the disturbance source is illustrated at the position of the controlling plasma actuator. The data has been obtained using a phase-

averaged hotwire technique. The amplitude distribution is resolved in spanwise direction (z-coordinate), as well as over the wall-normal direction (y-coordinate). The maximum amplitude has been adjusted to $A_{TS} \approx 1.0\%$ of the freestream velocity, which is considered to be still in the linear range of disturbance growth. It can be seen that the amplitude is not uniform over the spanwise direction. Two reasons are accountable for this behavior. A series deviation of the loudspeakers was found measuring the impedance of the single loudspeakers. This caused the amplitude to vary for each of them. By impedance matching of the loudspeakers, this effect could be reduced. Additionally, a customized amplifier has been built, which allows further matching of the signals by adjusting each loudspeaker through an individual potentiometer. Despite these measures, a non-uniformity as shown in Figure 4.12 remained. This variation can only be due to imperfections in the manufacturing process of the small orifices connecting each loudspeaker to the aerodynamic surface, as well as small variations in the geometry of the wing glove close to the leading edge. Nevertheless, a uniform amplitude exists in the range between $z = 180mm$ and $z = 300mm$, which covers the center line of the measurement area at $z = 200mm$ and all sensors positioned on the glove.

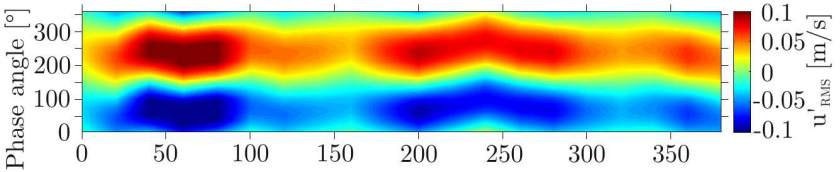

Figure 4.13: Spanwise phase angle distribution of incoming TS wave front.

Of equal importance as the amplitude is the phase variance of the generated disturbances along the spanwise direction. Figure 4.13 shows the phase angle of each point source in relation to the excitation signal fed to the amplifier. Again this data is obtained using a phase-averaged approach. Plotted is one averaged period of the disturbance signal taken at a wall-normal distance inside of the boundary layer, where the amplitude maximum is located. The measurement grid has been aligned with the geometry of the disturbance source, such that data points downstream of each point source and in between two point sources are available. The measurement shows that the uniformity of the phase angle is rather good in the spanwise direction and that the phase variation of the TS wave front stays

within acceptable limits. The result also proves that the assumption of a quasi two-dimensional wave front forming downstream of a row of point sources is valid if the spacing is chosen sufficiently small.

4.2.3 Transition Control Results, Single actuator, 1-D

Following the base flow investigations, a measurement campaign using a single controlling plasma actuator at $x/c = 0.337$ has been conducted. The experimental conditions have been set according to the description given in section 4.2.1. The results of these experiments have also been published in [41].

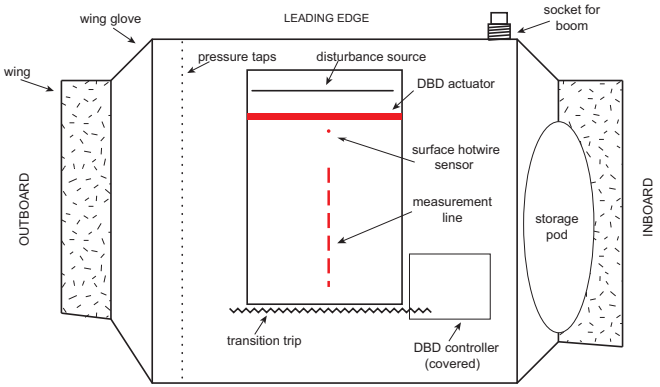

Figure 4.14: Schematic view of the setup using a single controlling plasma actuator. Measurements are taken in the center line of the inlay.

Three methods of transition control using plasma actuators have been applied in order to compare the transition control effect. These are boundary layer stabilization using a continuous mode of actuation, active wave control by amplitude modulation and the hybrid mode where continuous forcing and amplitude modulation are combined.

Figure 4.15 summarizes the most important results of the transition delay experiments at $Re = 0.94 \cdot 10^6$ and $\alpha = 1.0°$. This figure shows the RMS values of a hotwire signal, when the hotwire probe is traversed parallel to the wall at a wall-normal position of $y = 1.5mm$, which is the position of

maximum amplitude of the Tollmien-Schlichting waves within the boundary layer. In the transition region, the typical rise of the fluctuation amplitude is visible in the intermittency zone before u'_{RMS} settles to the level of turbulent flow. The streamwise locations where an amplitude of $u'_{RMS} = 1m/s$ is exceeded have been chosen to define the onset of transition for the various cases. For the base flow case (+), the boundary layer remains laminar over the complete measuring range. Only at the most downstream location, the RMS level begins to rise.

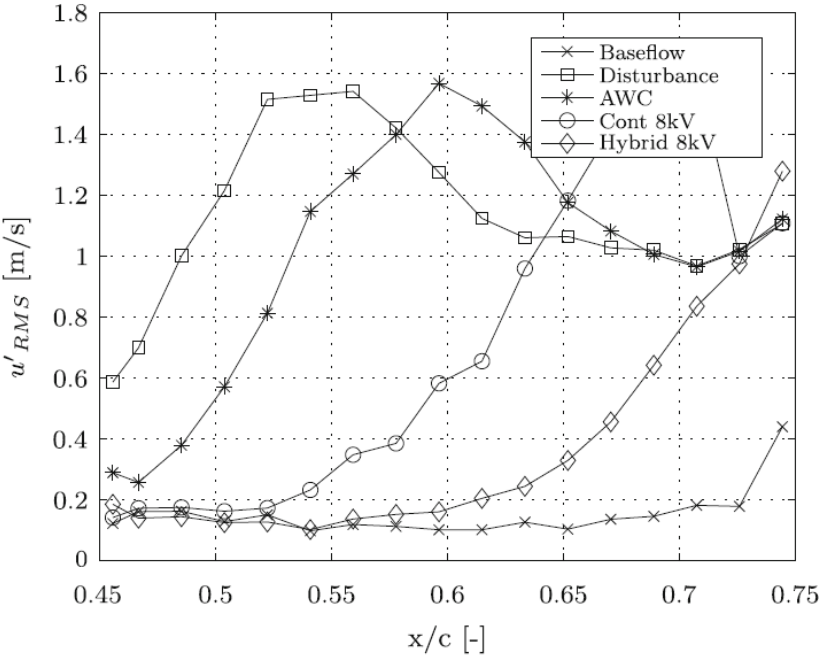

Figure 4.15: Downstream development of u'_{RMS} at a wall-normal position of $y = 1.5mm$ for the base flow, active wave control, continuous mode and hybrid mode at $V_{pp} = 8kV_{pp}$.

With the artificial disturbance source operating, the transition location moves upstream to $x/c = 0.485$ (□). For pure active wave cancelation with individually optimized parameters, the transition delay was $\Delta x/c = 0.047$ ($\star$), while operating the plasma actuator in a continuous fashion at $V_{pp} = 8kV_{pp}$, the transition delay amounts to $\Delta x/c = 0.152$ (○). Combining the

two methods with newly optimized parameters for the AWC, the transition region is moved downstream significantly further to $x/c = 0.727$ with a $\Delta x/c = 0.242$ ($\diamond$) and transition is still not complete at the end of the measurement region.

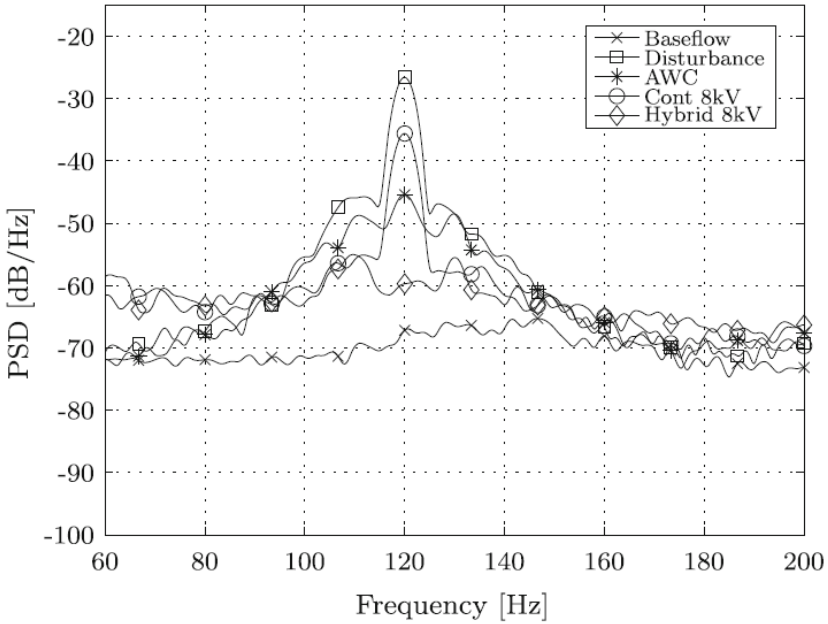

Figure 4.16: Power spectra of the error sensor signal ($y \approx 0mm$, $x/c = 0.391$) for the various cases.

Analyzing the power density spectra of the error sensor signal (Fig. 4.16) of a typical set of experiments reveals the achieved attenuation rates at the location of the error sensor. Operation of the disturbance source generates a clear peak in the spectrum with an amplitude of $L_{dB} = -26.6dB/Hz$ at the TS frequency of $f = 120Hz$ ($\square$). In hybrid mode of operation, a maximum reduction of $\Delta L_{dB} = -33.1dB/Hz$ is achieved ($\diamond$), which corresponds to an amplitude reduction of 97.8%, whereas active wave cancelation and continuous operation of the plasma actuator generate an intermediate amplitude reduction of 88.5% ($\star$) and 64.5% ($\circ$), respectively. Note that continuous actuation results in a more broadband attenuation as compared to pure active wave cancelation. This explains the fact that even though

the attenuation rate at the TS frequency in continuous mode is lower, a larger transition delay (Fig. 4.15) could be achieved.

Very interesting in this context is that the increased transition delay of the hybrid mode of operation is achieved without additional power consumption as compared to the continuous mode of operation. Continuous operation of this specific plasma actuator at a peak-to-peak voltage of $V_{pp} = 8kV_{pp}$ and a frequency of $f = 9.75kHz$ consumes a power of $P = 41.5W/m$. The additional (sinusoidal) modulation around this value for the combination with the active wave cancelation causes no measurable change in the average power consumption. The modulation needed for AWC merely appears as a slightly higher standard deviation in the time trace of the high voltage signal.

In this comparison the transition delay result of the hybrid transition control mode is evidently larger than the isolated effects of active wave control and continuous mode of operation. Two considerations are important in this context. It is assumed that an amplitude modulation while the actuator is running continuously, results in an even smoother counteracting disturbance signal than in the case of pure active wave control, where the actuator is "switched on and off". Even though a smooth amplitude oscillation is prescribed in this case as well, the response time of the oscillatory circuit during startup and shutdown is limited. Nevertheless, since the operating parameters for active wave control and hybrid mode have to be individually optimized in each case, a definite proof is not possible at this point and is left for future investigations. Secondly, a transition delay result with is larger than the sum of the isolated effects can be obtained if the amplitude of the excited unstable frequency is suppressed for a sufficient chordwise distance, such that transition by this frequency is overcome entirely. The unstable frequency band changes towards lower wave numbers towards the trailing edge of the airfoil and this modes appear later in the spectrum. This effect is certainly desired, but has to be attributed in part to the fact that artificial mono-frequency TS waves are considered here.

4.2.4 Transition Control Results, Two actuators, 2-D

After the promising results using a single plasma actuator, the setup has been modified for more detailed investigations. Using plasma actuators for active wave control as well as the boundary layer stabilization relies on a localized effect, were disturbances are damped directly or the boundary layer is stabilized impeding the growth of boundary layer disturbances for a

certain downstream distance. Nevertheless, in both cases the disturbances are amplified again downstream of the control location. Consequently, it should be possible to repeat the control to some extent to improve the transition delay result. To investigate this possibility, the setup has been modified for the use of two plasma actuators, which are operated with two independently acting controllers.

It was decided to apply feed-forward control for the subsequent experiments with the planned in-flight experiments in mind, since the adaptive control algorithm is capable of controlling TS waves of mixed frequency content and amplitude. A filtered-reference LMS algorithm as outlined in section 2.2.3 is utilized. To realize this setup three surface hotwire sensors have been installed, as illustrated in Figure 4.17. The hotwire in the center serves as error sensor for actuator 1 and at the same time as reference sensor for actuator 2.

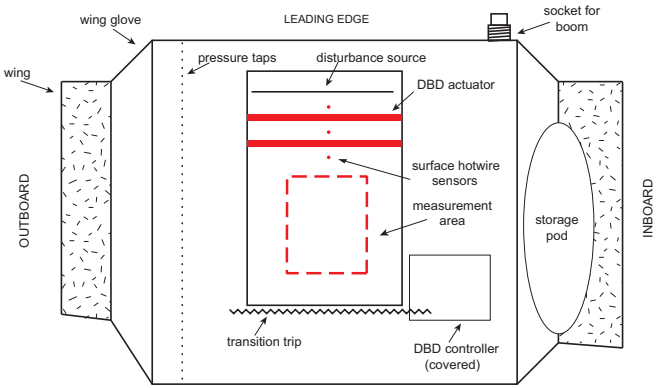

Figure 4.17: Schematic view of the setup using two controlling plasma actuators and three surface hotwires for feed-forward control.

Additionally, three-dimensional boundary layer measurements were planned in order to determine the uniformity of the transition location in the spanwise direction. A single hotwire has been traversed parallel to the curved surface of the wing glove at a wall-normal distance, where to maximum amplitude of the TS waves is located.

Figure 4.18 shows the applied measurement grid. In streamwise direction (x-coordinate) a resolution of $\Delta x = 20mm$ has been chosen. In spanwise

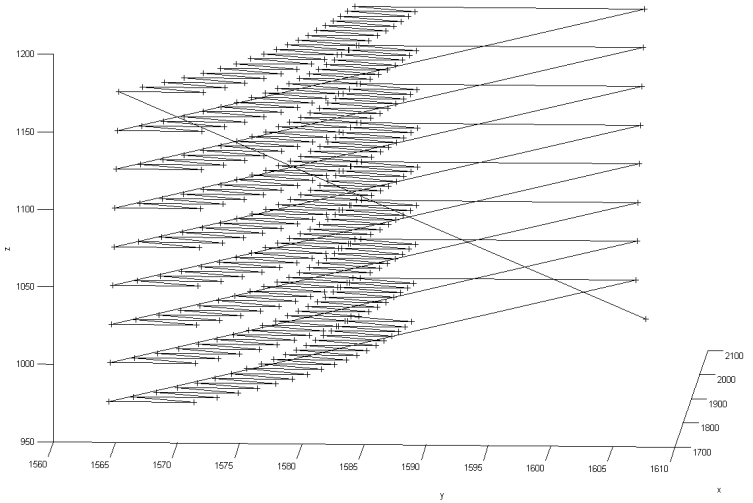

Figure 4.18: Measurement grid for two-dimensional transition location determination.

direction (z coordinate) the resolution is $\Delta z = 25mm$. The size of the field is $360mm \times 200mm$ in streamwise and spanwise direction, respectively. The hotwire signal has been acquired with a sampling rate of $20kHz$ for a duration of $2s$ at each point. The temporal resolution has to be chosen at least twice the highest expected frequency to avoid aliasing effects. The determining parameter in this case is the plasma actuator frequency of $f = 9.5kHz$. The relevant frequencies of the flow are expected in a range below $f = 2kHz$. To be able to judge the energy efficiency of the various transition control methods, detailed power measurements have been conducted, comparing active wave control, boundary layer stabilization and hybrid mode of operation.

Plotting the RMS value of each data point as contour plot results in a two-dimensional map of the transition region on the measurement inlay. Like previously described, the RMS value of the fluctuation signal (u')at each location can be utilized to indicate the onset of transition, where a sharp increase in the fluctuation amplitude is observed, before the signal is

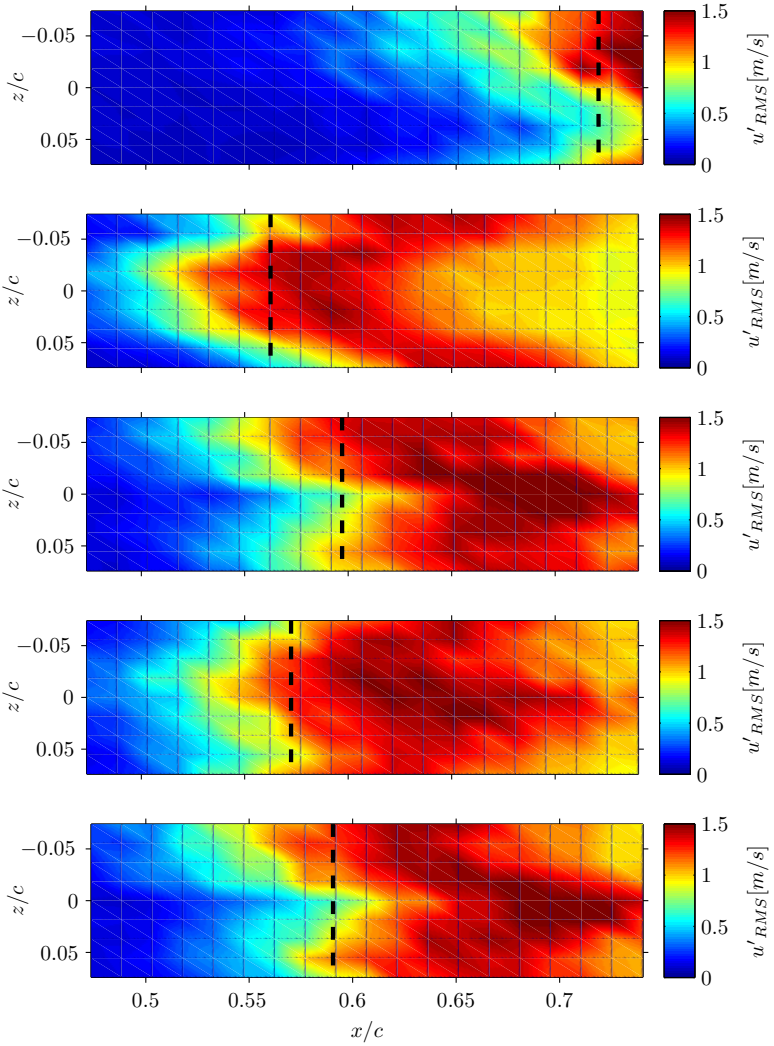

Figure 4.19: Average transition location on wing glove for active wave control. (Top to bottom: Base flow, forced base flow, upstream actuator, downstream actuator, both actuators operating.)

settling on the turbulent level. For each transition control method five of these plots are grouped together in order to be able to compare the individual cases. The order of the plots is consistent throughout this section. The ordering from top to bottom always shows base flow, activated disturbance source (forced base flow), forced base flow with the upstream plasma actuator operating alone (actuator 1), forced base flow with downstream actuator operating alone (actuator 2) and forced base flow with both controlling actuators operating at the same time. In the case when both actuators are operated simultaneously, they act independently of each other with individual control algorithms and sensors. Note that the spanwise direction is compressed by a factor of two in all plots.

Figure 4.19 summarizes the results for active wave control, which means the boundary layer disturbances are damped by linear negative superposition and the stability features of the boundary layer remain basically unchanged. Shown is the RMS value of the calibrated fluctuation signal u'_{RMS} as contour plot over streamwise and spanwise direction. The coordinates have been normalized with the chord length of the wing glove, which is $c = 1.35m$. The dashed line indicates the average transition location for the particular cases. The base flow transition occurs at $x/c = 0.719$ (Fig. 4.19(a)). Operation of the disturbance source moves the average transition location upstream to $x/c = 0.562$ (Fig. 4.19(b)). Active wave control using only the upstream plasma actuator yields a transition delay of $\Delta x/c = 3.5\%$ (Fig. 4.19(c)). Applying only the downstream actuator with individually optimized parameters, a transition delay of $\Delta x/c = 1.0\%$ could be obtained (Fig. 4.19(d)). Combining both actuators a transition delay of $\Delta x/c = 2.8\%$ is observed.

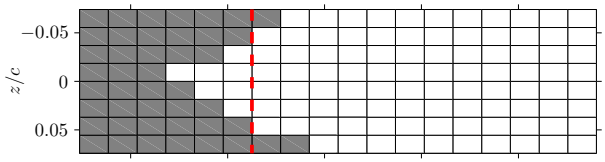

Figure 4.20: Determination of average transition location using the case of forced base flow as an example.

It is evident, that the achievable transition delay effect using only actuator 2, and also actuator 2 in combination with actuator 1, is small as compared to the performance of actuator 1 alone. This shows that for active

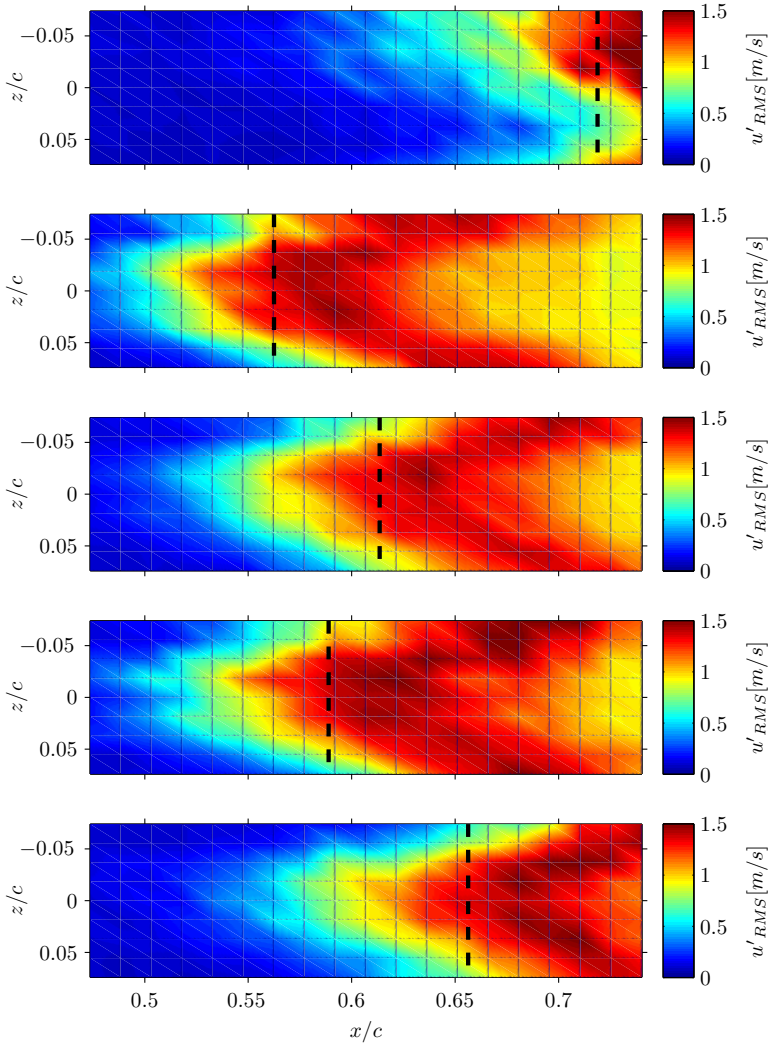

Figure 4.21: Average transition location for boundary layer stabilization. (Top to bottom: Base flow, forced base flow, upstream actuator, downstream actuator, both actuators operating.)

wave control the positioning of the controlling actuator is of fundamental importance. For an effective transition delay it is important that the actuator is placed in a location, where the TS amplitudes have been linearly amplified strong enough for the signal to be detected by the sensors, but the disturbances still have to be in their linear range of amplification. Once non-linear effects set in, the transition delay possible by the mechanism of negative linear superposition begins to reduce.

Using the case of the forced base flow as an example, the procedure of determining the average transition position is explained, as shown in Figure 4.20. A threshold of $u'_{RMS} = 1.0m/s$ has been chosen to locate the onset of transition. The flow upstream of this data point in the grid is considered laminar (dark panels), downstream of this location it is considered transitional or turbulent (white panels). The streamwise locations of the particular measurement points where the threshold is exceeded, are then averaged in order to obtain the average streamwise transition location.

In the next step the various cases have been obtained for pure continuous actuation without any amplitude modulation. This mechanism exploits the stabilizing effect of a continuous momentum input on the stability of the local boundary layer profile. For this mechanism it is known that a stabilizing effect is extending over a longer streamwise distance, and is less localized as in the case of active wave control.

For the base flow case the transition location is again located at $x/c = 0.719$. Operation of the disturbance source moves the transition location upstream to $x/c = 0.562$ (Fig. 4.21(a) and (b)). Continuous actuation of the upstream actuator (actuator 1) yields a transition delay of $\Delta x/c = 5.1\%$ (Fig. 4.21(c)). Individual continuous actuation the downstream located actuator 2 using the same voltage of ($V_{pp} = 8.0kV_{pp}$) results in a transition delay of $\Delta x/c = 2.6\%$ (Fig. 4.21(d)). In the case where both actuator are operated simultaneously (Fig. 4.21(e)), a transition delay of $\Delta x/c = 9.4\%$ is achieved.

For continuous actuation, the effect of the downstream actuator operating alone is still noticeably reduced, which indicates the sensitivity of the stabilizing effect on the positioning of the actuator in this case as well. Combining both actuators at the same power levels as during the cases of isolated operation, results in a transition delay that exceeds the sum of the individual effects. It should be noted that this transition delay result comes at a power consumption, which is in the order of four times higher as compared to active wave control.

In a subsequent set of experiments, the stabilizing effect of the continu-

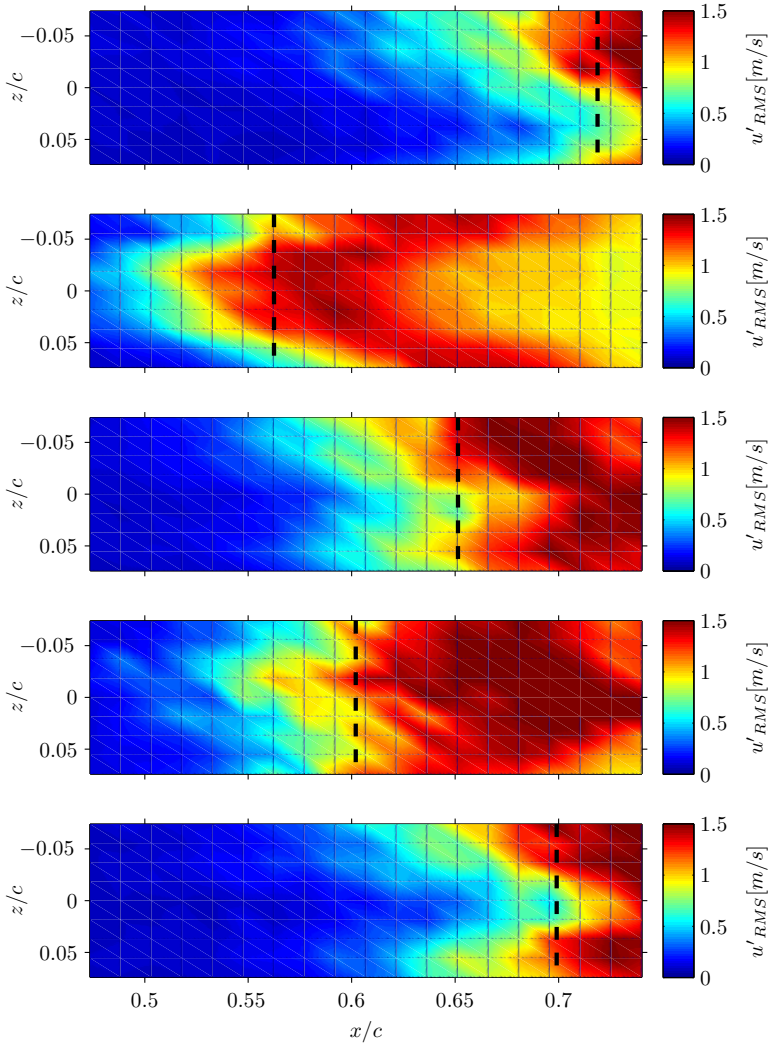

Figure 4.22: Average transition location on wing glove for hybrid control mode. (Top to bottom: Base flow, forced base flow, upstream actuator, downstream actuator, both actuators operating.)

ous actuation and direct disturbance damping using active wave cancelation have been combined in the hybrid mode of operation. The transition locations for base flow case and forced base flow with operating disturbance source are again given with $x/c = 0.719$ and $x/c = 0.562$ respectively, as shown in Figures 4.22(a) and (b). Applying hybrid transition control using only the upstream actuator (actuator 1) yields a transition delay of $\Delta x/c = 8.9\%$ (4.22(c)). The average high-voltage has been set to $V_{pp} = 8.0kV_{pp}$, the same value as in the cases of pure continuous action, which has been illustrated in Figure 4.21. With the individual operation of the downstream actuator (actuator 2) in hybrid mode at the same average high-voltage, a transition delay of $\Delta x/c = 4.0\%$ could be achieved (4.22(d)). Last but not least, the simultaneous operation of both actuators in hybrid mode using the same settings for the continuous operation, amounts to a transition delay of $\Delta x/c = 13.7\%$ (4.22(e)).

Overall, the hybrid mode of operation yields the highest absolute transition delay distances for all compared cases. No matter if the actuators are operated alone or simultaneously. The improved transition delay is achieved with similar energy consumption, as compared to pure continuous actuation. The additional amplitude modulation by the control algorithm around the preset average high-voltage, which has been $V_{pp} = 8.0kV_{pp}$ for all cases that include a continuous portion of forcing, does not modify the average power consumption significantly.

4.2.5 Power Consumption

In order to judge the control efficiency of the three methods, the consumed electrical power at each plasma actuator has been recorded for the various flow control cases. The data is sampled with a high rate of 500 kHz in order to obtain a good resolution of the individual discharge cycles.

Table 4.1: Power consumption for the various flow control cases per unit actuator length [W/m].

Actuator	AWC	CONT	HYBRID
PA 1	—	26.9	27.6
PA 2	4.7	18.7	16.9
PA1+PA2	—	43.9	44.7

Table 4.1 lists the results for the three applied flow control methods. PA1 refers to the actuator, which is located upstream, PA2 denotes the downstream actuator. In the case of transition control using both actuators simultaneously (PA1+PA2), the sum for both actuators is given.

Table 4.2: Transition delay performance $\Delta x/c$ [%].

Actuator	AWC	CONT	HYBRID
PA 1	—	0.19	0.32
PA 2	0.21	0.14	0.23
PA1+PA2	—	0.21	0.31

In Table 4.2 the control performance of continuous actuation, active wave control and hybrid mode is compared. The consumed power per unit actuator length is related to the transition delay $\Delta x/c$. Some of the power data for active wave control has been inconclusive, but it can be shown that in all three cases the control performance of the hybrid mode is significantly increased in comparison to a pure boundary layer stabilization by 48% to 68% for this particular setup and the chosen flow conditions.

5 Results of In-Flight Experiments

5.1 Base Flow Investigation

The flight experiment campaign has been divided into several subsequent steps. Following a thorough testing of all components of the instrumentation on the ground and during first flights, parameter studies have been conducted to define the desired operating conditions for the experiments. In a first approximation, dynamic pressure and angle of attack are proportional to each other during coordinated level flight if a constant take-off weight is assumed. The pressure gradient on the pressure side of the profile varies by design from favorable, over approximately zero, to destabilizing pressure gradients, depending on the operating conditions [62]. Therefore, the natural transition location is moving along x/c depending on the combination of angle of attack and flight Reynolds number. It is necessary to

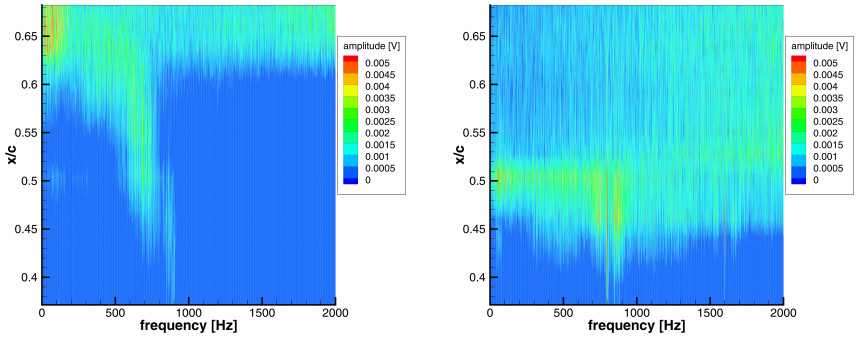

(a) Natural transition (base flow).

(b) Forced base flow ($f = 800Hz$).

Figure 5.1: Spectrogram of microphone array signals for base flow and forced transition at $Re = 3.0 \cdot 10^6$.

set an appropriate flow condition, because the natural transition location varies over a wide chord range for different conditions in the flight envelope

of the aircraft. A natural transition location has to be established, which is in the x/c range of the installed microphone array. During a parameter study, an angle of attack of $\alpha = 2.2°$ has been found suitable for the planed experiments. This corresponds to a Reynolds number based on chord of approximately $Re = 3.0 \cdot 10^6$.

In Figure 5.1 a spectrogram of the microphone array data is shown along the chord length for $Re = 3.0 \cdot 10^6$. A time interval of $1s$ has been chosen for the analysis. The most amplified naturally occurring frequencies (Fig. 5.1(a)) are in the range of $f = 600 - 900Hz$ at $x/c = 0.45$. The most unstable frequency range is decreasing with increasing chord length as expected, before a sudden widening of the spectrum can be observed at $x/c = 0.62$. The occurrence of a wide range of frequencies in the boundary layer is an indicator of turbulent flow.

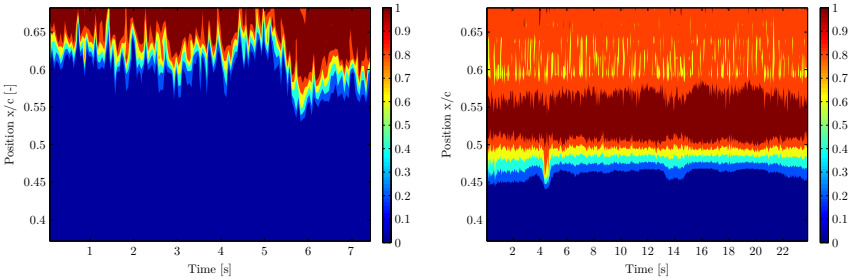

Figure 5.2: Time evolution of the transition location for base flow (left) and forced transition (right) at $Re = 3.0 \cdot 10^6$.

In a next step amplitude and frequency of the disturbance source have been varied in order to determine the settings for the forcing. A frequency of $f = 800Hz$ has been found to be the most effective, requiring the lowest amplitude at the disturbance source. Figure 5.1(b) shows the base flow case with forced transition. Besides the naturally occurring frequencies, a clear peak is visible at the forced frequency of $f = 800Hz$, which results in a transition location of $x/c = 0.45$.

Figure 5.2 shows the transition position in the center line of the wing glove over time for the base flow case and for base flow with forced transition. The RMS values of microphone array signals have been averaged over a time interval of $\Delta t = 0.1s$. Bandpass filtering has been applied due to issues with electromagnetic interference originating from the plasma actuator, as described in section 3.1.2.5. In Figure 5.2(a) the base flow case

transition position is shown over a sustained measurement time of $7.5s$. It can be seen that the natural transition position is located at approximately $x/c = 0.61$ on average, but is subject to large variations up to $\pm 5\%$. The large variance in the base flow case has several reasons. First of all, this flow state is sensitive to the freestream turbulence level and secondly, it is reacting already to small changes in the angle of attack. Changes in angle of attack can either be induced by the pilot or by gusts passing the airfoil, which can modify the effective angle of attack depending on their direction.

Figure 5.2(b) illustrates the conditions for base flow with running disturbance source over a continuous measurement time of $24s$. The average transition location is $x/c = 0.46$ with a variation of $\pm 2\%$. In this case the transition location is more predetermined due to the forcing and therefore less susceptible to other external disturbances.

5.2 Transition Control Experiments

Following the base flow analysis, transition control experiments have been conducted at the determined flow conditions ($Re = 3.0 \cdot 10^6$, $\alpha = 2.2°$). The three transition control methods, boundary layer stabilization, active wave control and hybrid mode of operation have been applied. A detailed descriptions of the underlying mechanisms and the working principles is given in section 2.1.3. The focus in the presented study is on active flow control using active wave cancelation and the hybrid mode of operation, nevertheless, the damping result of the stabilization in continuous mode of operation is of interest for comparison of the three methods.

5.2.1 Active Wave Cancelation

Figure 5.3(a) shows the fluctuation signal of surface hotwire 3 in active wave control mode for controlled and uncontrolled case. This flush-mounted hotwire is located at $x/c = 0.47$, which is approximately the position of the transition region with operating disturbance source, as previously shown in Figure 5.2(b)). Additionally to the fluctuation signal, the time dependent intermittency factor and the applied threshold is given. The graph represents a sustained measurement time of $14s$. The plot can be divided into three sections: base flow with forced transition but without control, active wave cancelation applied, and again base flow with forced transition.

At $t = 10.8s$ the control is applied, which causes the intermittency factor to drop substantially from values of $\gamma \approx 0.8$ to values below $\gamma = 0.1$, which

indicates that the transition region has moved downstream and surface hotwire 3 is now located in the laminar flow region. After shutdown of the control at $t = 18.2$, the intermittency factor returns to values of $\gamma \approx 0.8$. This indicates that the flow conditions have been stable throughout the measurement time.

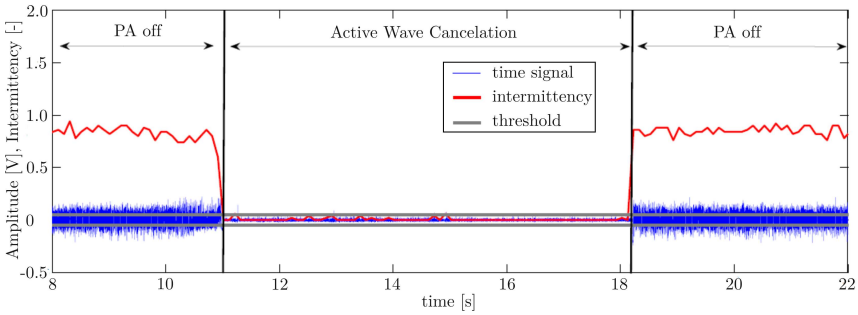

(a) Intermittency factor, corresponding threshold and fluctuation signal of surface hotwire 3.

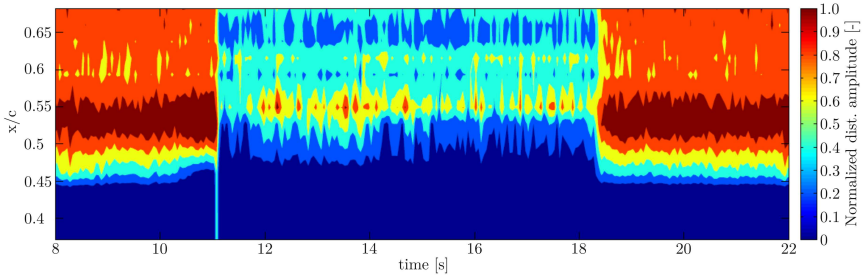

(b) Determination of transition location using RMS of microphone array signals.

Figure 5.3: Intermittency factor of surface hotwire 3 and corresponding RMS values of microphone array over time for active wave control.

Figure 5.3(b) shows the corresponding RMS levels of the microphone array showing the transition location over time. The microphone data is bandpass-filtered in the range of $f = 2.2 - 3.5kHz$ prior to the calculation of the RMS values, since the data has been subject to large interference with running plasma actuators in a frequency range below $f = 1.2kHz$ and

at the plasma actuators operating frequency of $f = 7.6kHz$. This resulted in a shift of the amplitude level during actuator operation, which makes a conclusive quantitative assessment of the transition delay difficult. A transition delay in the order of $x/c = 2 - 3\%$ is assumed from the data.

5.2.2 Boundary Layer Stabilization and Hybrid Transition Control

In a subsequent experiment the combined effect of boundary layer stabilization and active wave control has been investigated. The procedure for the measurement is such, that the training of the adaptive flow controller is conducted with constant plasma actuator forcing and added noise, which is introduced by a pseudo random bit stream (PRBS). The constant forcing has to be included in the modeling, since it modifies the time delay between signal generation at the plasma actuator and the impulse response at the error sensor. Also during a measurement the plasma actuator is started with continuous forcing, before the active wave control is added and its amplitude is adjusted by the controller to minimize the remaining disturbance amplitude.

Due to this predefined procedure, continuous and hybrid control always appear within the same measurement and can directly be compared. Figure 5.4(a) is showing the fluctuation signal of hotwire 3 located at $x/c = 0.47$, the corresponding intermittency factor, and the threshold that has been applied in a similar fashion as in section 5.2.1. The consecutive measurement time is $15s$ in this case.

In the uncontrolled case with operating disturbance source, the intermittency factor is approximately $\gamma = 0.8$, like in the previous experiment regarding active wave control. With continuous forcing starting at $t = 55s$, the intermittency factor is progressively reducing to values around $\gamma = 0.6$, until a large drop below $\gamma = 0.1$ is visible when the control is changed to the hybrid mode of operation combining boundary layer stabilization and active wave control. This proves two points: In both cases the flow control results in an amplitude reduction at $x/c = 0.47$ and the combination of boundary layer stabilization and active wave control strongly improves the damping result.

In terms of transition delay (Fig. 5.4(b)) a quantitative analysis is again difficult due to the electromagnetic interference in the microphone signal. Qualitatively, a transition delay of a few percent x/c is assumed for continuous forcing. This values are in accordance with the results of Duchmann

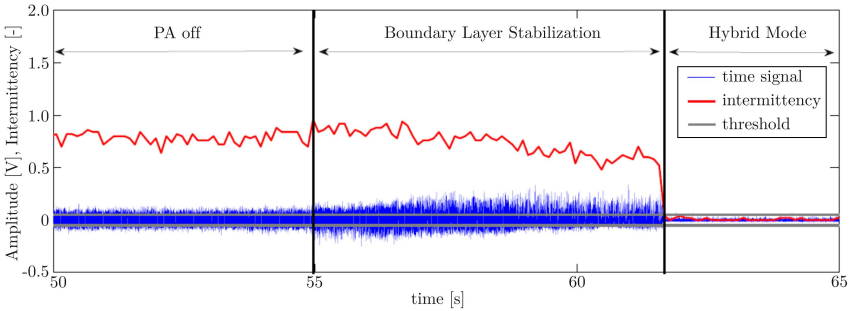

(a) Intermittency factor, corresponding threshold and fluctuation signal of surface hotwire 3.

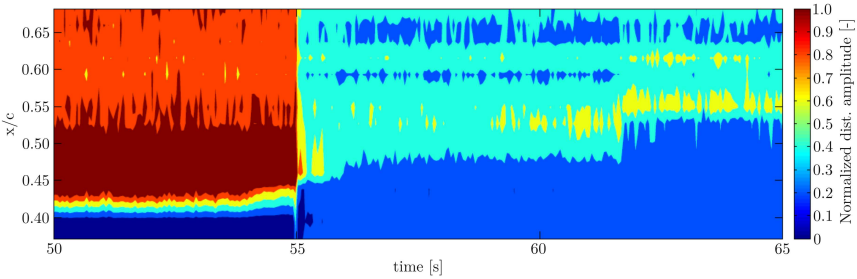

(b) Determination of transition location using RMS of microphone array signals.

Figure 5.4: Intermittency factor of surface hotwire 3 and corresponding RMS values of microphone array over time for hybrid control mode.

[16], who determined 3% transition delay for a comparable case.

Nevertheless, the relative transition delay increase between continuous and hybrid mode is assumed to yield dependable results, since the operating conditions of the plasma actuator and therefore the interference on the microphone array do not change significantly, when switching to hybrid mode of operation. The amplitude modulation of the operating voltage ($\Delta V_{pp} = \pm 0.5kV$) is small compared to the operating voltage of the plasma actuator, which is $V_{pp} = 11kV$ in this case. An additional transition delay of the same order ($x/c = 2 - 3\%$) is observed for the hybrid mode.

5.2.3 Conclusions

During the in-flight measurement campaign, the potential of the hybrid transition control method could be demonstrated. Either method, boundary layer stabilization and active wave control are limited in their achievable transition delay rates. In both cases an upper limit for the operating voltage exists, above which the transition delay cannot be improved, or is actually deteriorating. By combining both methods a substantial enhancement of the transition delay could be observed. These results have been obtained at a flight relevant Reynolds number of $Re = 3.0 \cdot 10^6$.

Unfortunately, the microphone array has been subject to electromagnetic interference issues, when operating the plasma actuator. In the given time for the in-flight measurement campaign, these problems could not be resolved, for example by a modified wire routing or additional electromagnetic shielding. This makes a definite quantification of the transition delay difficult. Nevertheless, a significant relative improvement between continuous mode and hybrid mode is assumed to be reliable from the obtained data and confirms the results of the wind tunnel experiments.

6 Conclusion

The goal of the present study is the improvement of the technological level using DBD plasma actuators for active disturbance control in the boundary layer of a laminar airfoil. Several subsequent steps have been undertaken in order to enhance the technique. A setup enabling experiments under realistic atmospheric turbulence conditions at Reynolds numbers relevant for small civil aircraft has been developed and successfully tested in a wind tunnel as well as in flight.

During the course of the investigations some interesting aspects using the DBD plasma actuator as flow control actuator have been investigated for the first time, which has lead to the development of the hybrid mode of operation. By the very nature of the momentum production of the plasma actuator this device is an ideal candidate to combine the positive effects of a local stability increase of the boundary layer, which acts on a broadband spectrum of unstable frequencies, with an energy efficient and instantaneous active wave cancelation.

In the following section a brief summary of the subsequent steps is given, combined with a discussion of the achieved results. The challenges that have been encountered allow for an objective outlook, judging the possibilities and necessities for further improvement.

6.1 Discussion

A crucial step in the beginning of the study was the development of an in-flight capable experimental setup, which can be utilized for fundamental research in the wind tunnel during the design phase and in flight on a motorized glider stationed at the local airfield. This newly developed setup allows for the investigation of advanced active flow control systems for boundary-layer disturbances under the influence of a pressure gradient and turbulent spectra, as they occur during atmospheric flight.

In the design phase of the experiment extensive wind tunnel campaigns have been conducted in order to probe the boundaries of the system. This included the question about the maximum achievable Reynolds numbers, at which effective transition control can still be obtained. It became clear

that even though the control authority of a DBD plasma actuator is limited, active wave control is nevertheless a promising application for this type of actuator, since the energy requirements to influence boundary layer instabilities in their early stage of development are small and the stability features of the boundary layer can be exploited.

During this phase of the project the possibility of combining boundary layer stabilization with an energy-effective active wave control has been successfully investigated. Boundary layer stabilization has relatively high energy requirements, but captivates by its capability to impede the growth of a broad band of unstable frequencies and to even delay transition initiated by naturally occurring, randomly distributed packets of TS waves using a two-dimensional actuator. This can be combined with a local active wave control, acting on the remaining disturbances in the boundary layer, which is energetically much more efficient. In fact the mean value of the actuators operating voltage is changed only minutely by the amplitude modulation necessary for the wave cancelation as compared to the pure boundary-layer stabilization procedure. This means that the transition delay result is improved with comparable energy requirements, which increases the energy efficiency of the method. Under wind tunnel conditions with lower free-stream velocities high transition delay rates of more than 20% of chord could be achieved.

The in-flight capability demanded a miniaturization and redesign of the complete electrical system, including the data acquisition system. In order to fulfill the requirements towards a significant increase of the Reynolds number, advanced feed-forward control algorithms have been applied in collaboration with the Technische Universität Berlin. It could be demonstrated, that the DBD plasma actuator can be used successfully for active wave control in flight. Also in this Reynolds number range relevant transition delay rates could be obtained.

6.2 Outlook

In order to further improve the method of active wave control in flight using DBD plasma actuators several suggestions can be made. Further efforts regarding the electromagnetic shielding of the electric system should be made in order to lower the detrimental effects of electromagnetic interference (EMI) originating from the high-voltage generators and the plasma actuators. Whereas the high-voltage generators and the wiring can be shielded effectively, the plasma actuators themselves act as a transmitter, which

cannot be avoided. Even though this has no influence on the transition process itself, the data acquisition equipment can be negatively influenced. For example the use of the microphone array to measure the transition location on the wing has been problematic due to high noise levels in the measurement signal during the operation of the actuators. Whereas this effect can be handled under wind tunnel conditions, the space constraints of an in-flight measurement setup intensifies these issues.

One possible solution could be the implementation of different measurement techniques. For example, the use of optical methods like the infrared (IR) thermography could prove useful in order to alleviate the EMI issues. An additional advantage of such a method is the instantaneous two-dimensional acquisition of the transition region. Since so far sensors are positioned locally on the wing, a spanwise observation of the transition region is necessary, since the control result might deteriorate with increasing distance to the sensors. This is even more important, if an attempt is made to control naturally occurring boundary layer instabilities.

For the control of natural transition a spanwise cascading of the plasma actuators will be necessary, due to the random spacing and occurrence of the TS wave packets. Even though boundary layer stabilization can be applied with a two-dimensional actuator also in this case, the active wave control is only applicable in close vicinity of the upstream flow sensors due to the limited spanwise extent of the disturbances and the spanwise variation of their amplitude in general. Certainly problematic will be the quickly increasing number of sensors and control circuits necessary. This goes hand in hand with a largely increased computational power.

In-flight transition experiments are much more involved in terms of complexity, cost and time requirements as compared to wind tunnel experiments, but from the experiences gained during the course of the presented study, they are certainly justified and worth while to be pursued in order to increase the technological level of flow control methods.

Bibliography

[1] T. Abe, Y. Takizawa, S. Sato, and N. Kimura. Experimental Study for Momentum Transfer in a Dielectric Barrier Discharge Plasma Actuator. *AIAA Journal*, 46(9):2248–2256, 2008.

[2] K. Barckmann. *Active Vortex Generation using Dielectric Barrier Discharge Plasma Actuators in Laminar Boundary Layers*. Dissertation, Technische Universität Darmstadt, 2013.

[3] M. Baumann. Aktive Dämpfung von Tollmien-Schlichting Wellen in einer Flügelgrenzschicht. *Fortschrittsberichte VDI*, Reihe 7, 1999.

[4] M. Baumann and W. Nitsche. Investigation of active control of Tollmien-Schlichting waves on a wing. In R. Henkes and J. van Ingen, editors, *Transitional Boundary Layers in Aeronautics*, volume 46, pages 89–98, 1996.

[5] N. Benard, J. Jolibois, A. Mizuno, and E. Moreau. Innovative three-electrode design for definition of multiple dielectric barrier discharge actuators. In *Electrostatic Joint Conference*, pages 1–17, 2009.

[6] N. Benard and E. Moreau. Electrical and mechanical characteristics of surface AC dielectric barrier discharge plasma actuators applied to airflow control. *Experiments in Fluids*, 55(11):1–43, 2014.

[7] J. P. Boeuf, Y. Lagmich, T. Challegari, and L. Pitchford. Electrohydrodynamic Force and Acceleration in Surfaces Discharges. In *AIAA 2006-3574, 37th AIAA Plasmadynamics and Lasers Conference*, San Francisco, California, USA, 2006.

[8] J. P. Boeuf, Y. Lagmich, and L. C. Pitchford. Contribution of positive and negative ions to the electrohydrodynamic force in a dielectric barrier discharge plasma actuator operating in air. *Journal of Applied Physics*, 106(2):023115, 2009.

[9] J. P. Boeuf, Y. Lagmich, T. Unfer, T. Callegari, and L. C. Pitchford. Electrohydrodynamic force in dielectric barrier discharge plasma actuators. *Journal of Physics D: Applied Physics*, 40(3):652–662, 2007.

[10] J. P. Boeuf and L. Pitchford. Electrohydrodynamic force and aerodynamic flow acceleration in surface dielectric barrier discharge. *Journal of Applied Physics*, 97(10):103307, 2005.

[11] U. Buder, A. Berns, J. von Klitzing, E. Obermeier, R. Petz, and W. Nitsche. Family of Micromachined Wall Hot-Wire Sensors on Polyimide Foil. *AIAA Journal*, 45(8):1798–1809, 2007.

[12] T. C. Corke, C. L. Enloe, and S. P. Wilkinson. Dielectric Barrier Discharge Plasma Actuators for Flow Control. *Annual Review of Fluid Mechanics*, 42(1):505–529, 2010.

[13] T. C. Corke, C. He, and M. P. Patel. Plasma Flaps and Slats: An Application of Weakly-Ionized Plasma Actuators. In *AIAA-2004-2127, 2nd AIAA Flow Control Conference*, Portland, Oregon, USA, 2004.

[14] A. Debien, N. Benard, and E. Moreau. Electric wind produced by sliding discharges. In *Proceedings of 2nd ISNPEDADM new electrical technologies for environment*, Nouméa, 2011.

[15] A. Debien, N. Benard, and E. Moreau. Streamer inhibition for improving force and electric wind produced by DBD actuators. *Journal of Physics D: Applied Physics*, 45:215201, 2012.

[16] A. Duchmann. *Boundary-Layer Stabilization with Dielectric Barrier Discharge Plasmas for Free-Flight Application*. Dissertation, Technische Universität Darmstadt, 2013.

[17] A. Duchmann, S. Grundmann, and C. Tropea. Delay of Natural Transition with Dielectric Barrier Discharges. *Experiments in Fluids*, 54(3), 2013.

[18] A. Duchmann, A. Kurz, A. Widmann, S. Grundmann, and C. Tropea. Characterization of Tollmien-Schlichting Wave Damping by DBD Plasma Actuators Using Phase-Locked PIV. In *AIAA 2012-0903, 50th AIAA Aerospace Sciences Meeting*, Nashville, Tennessee, USA, 2012.

[19] A. Duchmann, B. Simon, P. Magin, C. Tropea, and S. Grundmann. In-Flight Transition Control with DBD Plasma Actuators. In *AIAA 2013-0900, 51st AIAA Aerospace Sciences Meeting*, Grapevine, Texas, USA, 2013.

[20] S. Elliott. *Signal Processing for Active Control*. Signal Processing and its Applications. Academic Press, 2001.

[21] P. Erb. *Untersuchung der Grenzschichttransition im Flugversuch*. Dissertation, Technische Universität Darmstadt, 2002.

[22] G. I. Font. Boundary-Layer Control with Atmospheric Plasma Discharges. *AIAA Journal*, 44(7):1572–1578, 2006.

[23] M. Forte, J. Jolibois, E. Moreau, G. Touchard, and M. Cazalens. Optimization of a Dielectric Barrier Discharge Actuator by Stationary and Non-stationary Measurements of the Induced Flow Velocity - Application to Airflow Control. In *AIAA 2006-2863, 3rd AIAA Flow Control Conference*, San Francisco, California, USA, 2006.

[24] M. Forte, J. Jolibois, J. Pons, E. Moreau, G. Touchard, and M. Cazalens. Optimization of a Dielectric Barrier Discharge Actuator by Stationary and Non-Stationary Measurements of the Induced Flow Velocity: Application to Airflow Control. *Experiments in Fluids*, 43(6):917–928, 2007.

[25] M. Forte, L. Leger, J. Pons, E. Moreau, and G. Touchard. Plasma actuators for airflow control: measurement of the non-stationary induced flow velocity. *Journal of Electrostatics*, 63(6):929–936, 2005.

[26] J. H. Fransson, M. Matsubara, and P. H. Alfredsson. Transition induced by free-stream turbulence. *Journal of Fluid Mechanics*, 527:1–25, 2005.

[27] G. Gelbert, J. Moeck, C. Paschereit, and R. King. Advanced algorithms for gradient estimation in one- and two-parameter extremum seeking controllers. *Journal of Process Control*, 22:700–709, 2012.

[28] N. Goldin. *Widerstandsreduktion durch laminare Strömungskontrolle: Direkte und bionische Verfahren*. Dissertation, Technische Universität Berlin, 2013.

[29] N. Goldin and R. King. Learning from dolphin skin - drag reduction by active delay of transition flow control by distributed wall actuation. In *Notes on Numerical Fluid Mechanics and Multidisciplinary Design*, volume 119, pages 207–222. Springer, 2012.

[30] S. Grundmann. *Transition Control using Dielectric Barrier Discharge Actuators*. Dissertation, Technische Universität Darmstadt, 2008.

[31] S. Grundmann, S. Klumpp, and C. Tropea. Experimental and numerical investigations of boundary-layer influence using plasma-actuators. *Notes on Numerical Fluid Mechanics and Multidisciplinary Design (NNFM)*, 95:56–68, 2007.

[32] S. Grundmann and C. Tropea. Active Cancellation of Artificially Introduced Tollmien-Schlichting Waves using Plasma Actuators. *Experiments in Fluids*, 44(5):795–806, 2007.

[33] S. Grundmann and C. Tropea. Experimental Transition Delay Using Glow-Discharge Plasma Actuators. *Experiments in Fluids*, 42(4):653–657, 2007.

[34] S. Grundmann and C. Tropea. Experimental Damping of Boundary-Layer Oscillations using DBD Plasma Actuators. *International Journal of Heat and Fluid Flow*, 30(3):394–402, 2009.

[35] E. Hänsler and G. Schmidt. *Acoustic Echo and Noise Control: A Practical Approach*. John Wiley & Sons, 2004.

[36] L. Henning, R. Becker, G. Feuerbach, R. Muminovic, R. King, A. Brunn, and W. Nitsche. Extensions of adaptive slope-seeking for active flow control. *Proceedings of the Institution of Mechanical Engineers, Part I: Journal of Systems and Control Engineering*, 222(5):309–322, 2008.

[37] T. N. Jukes and K.-S. Choi. Flow control around a circular cylinder using pulsed dielectric barrier discharge surface plasma. *Physics of Fluids*, 21(8):084103, 2009.

[38] T. N. Jukes and K.-S. Choi. Dielectric-barrier-discharge vortex generators: characterisation and optimisation for flow separation control. *Experiments in Fluids*, 52(2):329–345, 2012.

[39] T. N. Jukes, T. Segawa, and H. Furutani. Active Flow Separation Control on a NACA 4418 using DBD Vortex Generators and FBG Sensors. In *AIAA 2012-1139, 50th AIAA Aerospace Sciences Meeting including the New Horizons Forum and Aerospace Exposition*, Nashville, Tennessee, USA, 2012.

[40] J. Kriegseis. *Performance Characterization and Quantification of Dielectric Barrier Discharge Plasma Actuators*. Dissertation, TU Darmstadt, 2011.

[41] A. Kurz, N. Goldin, R. King, C. Tropea, and S. Grundmann. Hybrid transition control approach for plasma actuators. *Experiments in Fluids*, 54(1610), 2013.

[42] E. Moreau. Airflow Control by Non-Thermal Plasma Actuators. *Journal of Physics D: Applied Physics*, 40(3):605–636, 2007.

[43] E. Moreau, R. Sosa, and G. Artana. Electric wind produced by surface plasma actuators: a new dielectric barrier discharge based on a three-electrode geometry. *Journal of Physics D: Applied Physics*, 41(11):115204, 2008.

[44] W. Nitsche and A. Brunn. *Strömungsmesstechnik*. VDI-Buch. Springer, 2nd edition, 2006. ISBN 978-3-540-32487-4.

[45] W. Nitsche, J. Suttan, S. Becker, P. Erb, M. Kloker, and C. Stemmer. Experimental and numerical investigations of controlled transition in low-speed free flight. *Aerospace Science and Technology*, 5(4):245–255, 2001.

[46] I. Peltzer. Comparative in-flight and wind tunnel investigation of the development of natural and controlled disturbances in the laminar boundary layer of an airfoil. *Experiments in Fluids*, 44(6):961–972, 2008.

[47] I. Peltzer, A. Pätzold, and W. Nitsche. In-flight experiments for delaying laminar-turbulent transition on a laminar wing glove. *Proceedings of the Institution of Mechanical Engineers, Part G: Journal of Aerospace Engineering*, 223(6):619–626, 2009.

[48] J. Perraud. *Description et mode d' emploi du code CASTET*. ONERA, RT ONERA/DERAT 124/5118.32, 1997.

[49] J. Perraud, O. Vermeersch, and R. Houdeville. *Descriptif et mode d' emploi du code 3C3D*. ONERA, RT 1/18325 DMAE, 2011.

[50] A. Reeh, M. Weissmüller, and C. Tropea. In-Flight Investigation of Transition Under Turbulent Conditions on a Laminar Wing Glove. *AIAA Journal*, 52(10):2176–2189, 2014.

[51] J. R. Roth, D. Sherman, and S. P. Wilkinson. Boundary Layer Flow Control with a One Atmosphere Uniform Glow Discharge Surface Plasma. In *AIAA 1998-0328, 36th AIAA Aerospace Science Meeting and Exhibit*, Reno, Nevada, USA, 1998.

[52] R. J. Roth, D. M. Sherman, and S. P. Wilkinson. Electrohydrodynamic Flow Control with a Glow-Discharge Surface Plasma. *AIAA Journal*, 38(7):1166–1172, 2000.

[53] H. Schlichting and K. Gersten. *Grenzschicht-Theorie*. Springer-Verlag, 2005.

[54] J. Schulze. Numerical Simulation of Various Flow Conditions on the G109b Research Aircraft. Bachelor thesis, Technische Universität Darmstadt, 2010.

[55] A. Séraudie, E. Aubert, N. Naude, and J. P. Cambronne. Effect of plasma actuators on a flat plate laminar boundary layer in subsonic conditions. In *AIAA 2006-3350, 3rd AIAA Flow Control Conference*, San Francisco, California, USA, 2006.

[56] A. Séraudie, O. Vermeersch, and D. Arnal. DBD Plasma actuator effect on a 2D model laminar boundary layer. Transition delay under ionic wind effect. In *AIAA 2011-3515, 29th AIAA Applied Aerodynamics Conference*, Honolulu, Hawaii, USA, 2011.

[57] D. Sturzebecher and W. Nitsche. Active cancellation of Tollmien-Schlichting instabilities on a wing using multi-channel sensor actuator systems. *International Journal of Heat and Fluid Flow*, 24(4):572–583, 2003.

[58] T. Unfer and J. P. Boeuf. Modeling and comparison of sinusoidal and nanosecond pulsed surface dielectric barrier discharges for flow control. *Plasma Physics and Controlled Fusion*, 52(12):124019, 2010.

[59] H. R. Velkoff and J. Ketcham. Effect of an Electrostatic Field on Boundary-Layer Transition. *AIAA Journal*, 6(7):1381–1383, 1968.

[60] D. Vieira. *Numerical simulation of aerodynamic plasma actuator effects*. Dissertation, Technische Universität Darmstadt, 2013.

[61] A. N. Vorobiev, R. M. Rennie, E. J. Jumper, and T. E. McLaughlin. Experimental Investigation of Lift Enhancement and Roll Control Using Plasma Actuators. *Journal of Aircraft*, 45(4):1315 – 1321, 2008.

[62] M. Weismüller. *A new Approach to Aerodynamic Performance of Aircraft under Turbulent Atmospheric Conditions*. Dissertation, Technische Universität Darmstadt, 2012.

[63] B. Wilke. *Aerodynamische Strömungssteuerung mittels dielektrischen Barriereentladungs-Plasmaaktuatoren.* Dissertation, Technische Universität Darmstadt, 2009.

[64] D. H. Zhang, Y. T. Chew, and S. H. Winoto. Investigation of intermittency measurement methods for transitional boundary layer flows. *Experimental Thermal and Fluid Science*, 12(4):433–443, 1996.

Nomenclature

Latin letters

upper case

symbol	SI unit	description
A_{TS}	–	amplitude of Tollmien-Schlichting waves
C_p	–	drag coefficient
D	m	diameter
F	N/m^3	integral body force
$G(q)$	–	plant response
G_e	–	secondary (error) path
$\hat{G}(q)$	–	estimated plant response
H	–	overall control transfer function
H_{12}	–	shape factor
I	–	number of controller coefficients
J	–	cost function
K	–	step size parameter
N	–	N-factor
P	W	power
P_e	–	primary (disturbance) path
Re	–	Reynolds number
Tu	–	turbulence level
U_∞	m/s	freestream velocity
U	m/s	velocity
V	V	voltage
V_{pp}	V	peak-to-peak voltage

lower case

symbol	SI unit	description
c	–	(control) actuator
c	m	chord length
d	–	disturbance signal
$\hat{d}$	–	estimated disturbance signal
e	–	error sensor, error signal
h	–	impulse response coefficients
q'	–	fluctuation
$\hat{q}$	–	amplitude function
r	–	reference sensor
t	s	time
u	–	control signal
u'	m/s	velocity fluctuation
v	–	modulated input signal
w	–	impulse response coefficients
x	–	reference signal
x	m	chordwise coordinate
y	–	output signal
y	m	wall normal coordinate
z	m	spanwise coordinate

Greek letters

upper case

symbol	SI unit	description
Δt	s	time interval
Ω	rad/s	frequency

lower case

symbol	SI unit	description
α	$^\circ$	angle of attack
α	–	convergence coefficient
$\tilde{\alpha}$	–	normalized convergence factor
α_i	–	spatial amplification rate
α_r	–	wave number
β	–	spanwise wave number
γ	–	intermittency factor
δ	–	Kronecker delta function
δ_1	m	displacement thickness
δ_2	m	momentum thickness
μ	–	convergence factor
ϕ	rad,$^\circ$	phase angle

Abbreviations

symbol	description
AC	alternating current
A/D	analog to digital
AOA	angle of attack
AWC	active wave cancelation
CA	continuous actuation
CTA	constant temperature anemometry/anemometer
DBD	dielectric barrier discharge
DC	direct current
DFG	Deutsche Forschungsgemeinschaft
DS	disturbance source
EKF	extended Kalman filter
EMI	electromagnetic interference
ESC	extremum-seeking control
FIR	finite impulse reponse
filtered-x LMS	filtered-reference least mean square
GPS	global positioning system
HV	high voltage
IR	infra-red
LDA	laser doppler anemometry/anemometer
LMS	least mean square
LSA	linear stability analysis
LTI	linear time-invariant
NACA	National Advisory Committee for Aeronautics
NI	National Instruments
NWK1	Niedergeschwindigkeits-Windkanal 1
ONERA	Office national d'études et de recherches aérospatiales
PA	plasma actuator
PIV	particle image velocimetry
PMMA	polymethyl methacrylate
PRBS	pseudo-random binary sequence

PSD	power spectral density
RMS	root mean square
RT	real-time
SISO	single-in-single-out
SNR	signal-to-noise ratio
SNS	sensor
TS	Tollmien-Schlichting
TTL	transistor-transistor logic
UAV	unmanned aerial vehicle
2D	two-dimensional
3D	three-dimensional

List of Figures

List of Tables